

# The design of Pd-containing high-entropy alloys and their hardening behavior under He ion irradiation



Shangkun Shen<sup>a,1</sup>, Liyu Hao<sup>a,1</sup>, Xing Liu<sup>a</sup>, Yufei Wang<sup>a</sup>, Yingxi Li<sup>b</sup>, Jian Zhang<sup>c</sup>, Engang Fu<sup>a,\*</sup>

<sup>a</sup> State Key Laboratory of Nuclear Physics and Technology, Department of Technical Physics, School of Physics, Peking University, Beijing 100871, China

<sup>b</sup> School of Nuclear Science and Engineering, Shanghai Jiao Tong University, Shanghai 200240, China

<sup>c</sup> College of Energy, Xiamen University, Xiamen 361005, China

## ARTICLE INFO

### Keywords:

He ion irradiation  
High-entropy alloy  
Pd alloying  
He bubble  
Irradiation-induced hardening

## ABSTRACT

Imparting additional chemical heterogeneities of high-entropy alloys (HEAs) is considered as a novel strategy to improve their irradiation resistance on dislocation loop growth; however, there is still a lack of knowledge about the effects of this strategy on bubble evolution and irradiation-induced hardening. In this study, a series of Pd-containing FeCrNiCo HEAs with proven potential for chemical short-range order were designed and irradiated by 400 keV He ions to the fluences of  $5 \times 10^{16} \text{ cm}^{-2}$ ,  $1 \times 10^{17} \text{ cm}^{-2}$ , and  $5 \times 10^{17} \text{ cm}^{-2}$  at 723 K. Microscopic characterization demonstrates a remarkably inhibited growth of dislocation loops and promoted bubble coarsening in the Pd-containing HEAs compared to the HEA without Pd alloying. The underlying mechanism is that although the alloying of Pd can suppress the evolution of dislocation loops through severe local lattice distortion, it also significantly reduces the vacancy formation energy of the entire HEA system, leading to the encouraged bubble evolution. Pd-containing HEAs exhibit improved resistance to irradiation-induced hardening at low doses, but this advantage is unexpectedly absent with increasing dose. The hardening mechanism is explained by identifying the loop-dominated hardening at low dose and the bubble-induced hardening which makes an increased contribution at high dose. In addition, the Ni segregation around bubbles and loop punching mechanism are also discussed to provide essential evidence. These insights can help to shed light on the effects of Pd alloying on bubble evolution and irradiation-induced hardening behavior in HEAs, and thus contribute to the design of irradiation-resistant HEAs.

## 1. Introduction

The service performance and lifetime of the structural materials exposed to prolonged irradiation at elevated temperature directly determine the safe and long-term operation of nuclear reactors [1,2]. The extremely harsh environments in nuclear reactors invariably cause severe degradation of structural integrity and performance of the materials, such as void swelling [3,4], irradiation-induced hardening and embrittlement [5,6]. Therefore, the design of structural materials that can survive in extreme conditions is a critical challenge for the development and application of advanced nuclear systems.

Driven by these demands, a class of high-entropy alloys (HEAs) composed of various transitional metal elements have received much attention due to their improved irradiation resistance [7,8]. Among them, a variety of HEA systems based on the Cantor alloy [9,10]

( $\text{Fe}_{20}\text{Cr}_{20}\text{Mn}_{20}\text{Ni}_{20}\text{Co}_{20}$ ) have been considered to be one of the most promising structural materials in the future nuclear systems. However, the ubiquitous Co in Cantor alloys is a highly neutron-activated element that would have long-term adverse effects on the environment [11]. In terms of HEA design for irradiation-resistant purpose, hence, it is necessary to meet the strict requirements of irradiation resistance, and also to select components with low activation (replacing the Co in Cantor alloy with other viable elements).

Recently, several Pd-containing HEAs have attracted great interest and been verified to exhibit peculiar properties that are different from the HEAs belonging to the conventional Cantor-alloy category. For example, Ding et al. [12] reported that a new quinary  $\text{FeNiCoCrPd}$  HEA shows inhomogeneous characteristics in a local chemical environment and thus exhibits significantly enhanced mechanical strength compared to that of Cantor alloy at a similar grain size. Subsequently, Tran et al.

\* Corresponding author.

E-mail address: [efu@pku.edu.cn](mailto:efu@pku.edu.cn) (E. Fu).

<sup>1</sup> These authors contributed equally to this work.

[13,14] conducted simulation studies of several HEAs alloying with Pd/Mn. Their works verified the local chemical fluctuation in FeNi-CoCrPd, which provided explanations of Ding's study. In addition, Pd-containing Cantor alloys also emerged in the irradiation-resistant HEAs, which exhibited obviously improved irradiation resistance. Specifically, Yang et al. [15] investigated the void swelling in NiCoFeCr alloying with several different elements under the condition of 3 MeV Ni ion irradiation, and their results demonstrated that alloying with Pd in Ni-based HEAs could effectively delay the growth of dislocation loops and voids compared to alloying with Mn at high temperatures. Lu et al. [16] reported that the smaller dislocation loop size and higher loop density were observed in NiCoFeCrPd than those of NiCoFeCrMn irradiated by Ni ions, which is due to the higher local lattice distortion in NiCoFeCrPd. Similarly, Tong et al. [17] proposed that the strong mean local lattice distortion in Pd-HEA could inhibit the growth of dislocation loops at low irradiation doses. In terms of energetics, recently, Zhao et al. [18] pointed out that doping Al, Cu, Pd or Ti minor impurities in the CoCrFeNi HEA matrix would reduce the vacancy formation energy while increasing the migration energy of point defects, indicating a possible strategy to improve irradiation resistance of HEAs in CoFeNi-system.

The above existing studies mainly focus on the evolution of dislocation loops and voids under the condition of heavy-ion irradiation; however, there is still a lack of knowledge about the effects of Pd alloying on irradiation-induced hardening and bubbles evolution in these HEAs under the condition of He ion irradiation. Moreover, the strategy of removing Co and replacing it with Pd in Cantor alloys still needs further demonstration, which is significant for the design and development of Co-free and Pd-containing HEAs with guaranteed irradiation resistance in advanced nuclear systems. In this study, a series of  $(\text{FeCrNi})_{75}\text{Co}_{25-x}\text{Pd}_x$  ( $x = 0, 5, 15, 25$ ) HEAs were carefully prepared and irradiated with 400 keV He ions to the fluences of  $5 \times 10^{16}$  ions/cm<sup>2</sup>,  $1 \times 10^{17}$  ions/cm<sup>2</sup>, and  $5 \times 10^{17}$  ions/cm<sup>2</sup> at 723 K. The He bubbles were characterized by cross-sectional transmission electron microscopy (TEM), and the hardness of the four samples before and after irradiation was measured by using nanoindentation. Furthermore, first-principles calculations were carried out to obtain the vacancy formation energy, interaction energy between He interstitials and vacancies, and interstitial migration energy. The effect of Pd content on bubble evolution and the hardening mechanism were systematically analyzed, and the role of potential chemical short-range order and component differences of HEAs on irradiation defects was revealed. These insights provide experimental data and theoretical basis for the design of Pd-containing HEAs for the development of the irradiation-resistant materials.

## 2. Methods

### 2.1. Sample preparation and He ion irradiation

The four types of experimental samples based on  $(\text{FeCrNi})_{75}\text{Co}_{25-x}\text{Pd}_x$  ( $x = 0, 5, 15, 25$ ) HEAs were designed and used in this study. Fe, Cr, Ni, Co and Pd raw materials (>99.99 % purity) were accurately weighed and mixed via arc-melting and suction casting method with electromagnetic stirring. To ensure the homogeneity of all the components, the ingots were re-melted at least five times before being suction casted into a copper mold. Then the ingots were annealed at 1453 K for 24 h to eliminate possible component segregation and to exhibit coarse

grains. The specific compositions of the four samples are shown in Table 1. In the following, these samples are denoted as 0Pd, 5Pd, 15Pd, and 25Pd, respectively, according to their Pd contents. The as-received four types of HEAs were cut into thin slices with a thickness of 1 mm and electrochemically polished to the mirror face. Among them, the two mixed solutions were used for electrochemically polishing: 10 % perchloric acid ethanol for the 0Pd sample at 273 K, and 16 % perchloric + 42 % acetic + 42 % butoxyethanol for the Pd-containing samples at 263 K.

The polished samples were irradiated by 400 keV He ions to the fluences of  $5 \times 10^{16}$  ions/cm<sup>2</sup>,  $1 \times 10^{17}$  ions/cm<sup>2</sup>, and  $5 \times 10^{17}$  ions/cm<sup>2</sup> at 723 K ( $\sim 0.45 T_m$ .  $T_m$  is the melting point of the HEAs in this study). The irradiation experiments were performed on a 400 kV NEC ion implanter at Xiamen University (Xiamen, China). During the irradiations, the dose rate was set to approximately  $8 \times 10^{12}$  ions/cm<sup>2</sup>·s with an ion beam spot size of Φ3 cm, and the slow heating rate was controlled to 1 K per 10 s with vacuum in the target chamber maintained at  $10^{-5}$  Pa. In addition, the corresponding displacements per atom (dpa) and He concentration as a function of depth were simulated by using SRIM-2013 (Stopping and Ranges of Ions in Matter) program in quick Kinchin-Pease mode with the displacement threshold energy ( $E_d$ ) of 34 eV for Pd element and 40 eV for other elements [19,20], and the simulation results of the four HEAs are shown in Fig. 1.

### 2.2. Characterization

The phase structures of the pristine samples were identified by X-ray diffraction (XRD, Panalytical Empyrean with Cu K-alpha radiation) operated at 45 kV and 40 mA. The range of scanning angle ( $2\theta$ ) was set from  $35^\circ$  to  $100^\circ$  with a step size of  $0.005^\circ$ . Furthermore, the wavelength of the X-ray was carefully calibrated with standard Si sample before the tests, so that the lattice constants of the four HEAs can be estimated by Bragg's law.

The cross-sectional microstructures of the samples after irradiation were characterized by using TEM (FEI Cs corrected Titan Cubed Themis G2 operated at 300 kV with convergence semi-angle of 23.5 mrad) in bright field (STEM-BF) and high-angle annular dark field (STEM-HAADF) imaging mode. Specifically, the irradiation-induced dislocation loops were observed using the on-zone STEM-BF [21] characterization strategy, which has been found to be particularly effective at excluding most of the background contrast caused by thickness fringes and improving image imaging quality of irradiation defects. TEM-BF was applied with both over-focus and under-focus methods to observe bubbles to exclude complex contrast. The collected atomic-resolution HAADF images were processed with the Nion-Swift code to highlight the meaningful features. Simultaneously, the energy dispersive spectroscopy (EDS) with low beam current and long dwell time was adopted to analyze the chemical composition of the samples.

The thin foils used for the above TEM analysis were prepared by using the focused ion beam (FIB) lift-out technique on a FEI Helios G4 workstation. During the FIB process, the Ga ions at 30 kV (current range of 0.77–9.1 nA) were used to lift and thin the foils, and the final milling was performed at 2 kV (current of 44 pA) to remove amorphous layer and unexpected damage introduced by the thin process. The size and density of He bubbles were counted in the Nano-measurer software, and the thickness of the obtained foils was measured to be  $\sim 55$  nm via high energy-resolution electron energy loss spectroscopy (EELS) on a Cs corrected Nion U-HERMES200 STEM operated at 60 kV at Peking university, which was used for the calculation of number density (in m<sup>-3</sup>) of the bubbles and dislocation loops. To ensure the reliability of the statistical results, the size and number density data for each sample were collected from at least ten TEM/STEM images. In addition, nano-indentation tests were conducted on a Nano Indenter (G200, Agilent) to evaluate the irradiation-induced hardening of the samples by using continuous stiffness measurement (CSM) with the Berkovich-type indenter, and the average hardness data of each sample was obtained

**Table 1**

Chemical compositions (at.%) of the four types of  $(\text{FeCrNi})_{75}\text{Co}_{25-x}\text{Pd}_x$  HEAs.

Elements	Fe	Cr	Ni	Co	Pd
0Pd	25	25	25	25	0
5Pd	25	25	25	20	5
15Pd	25	25	25	10	15
25Pd	25	25	25	0	25

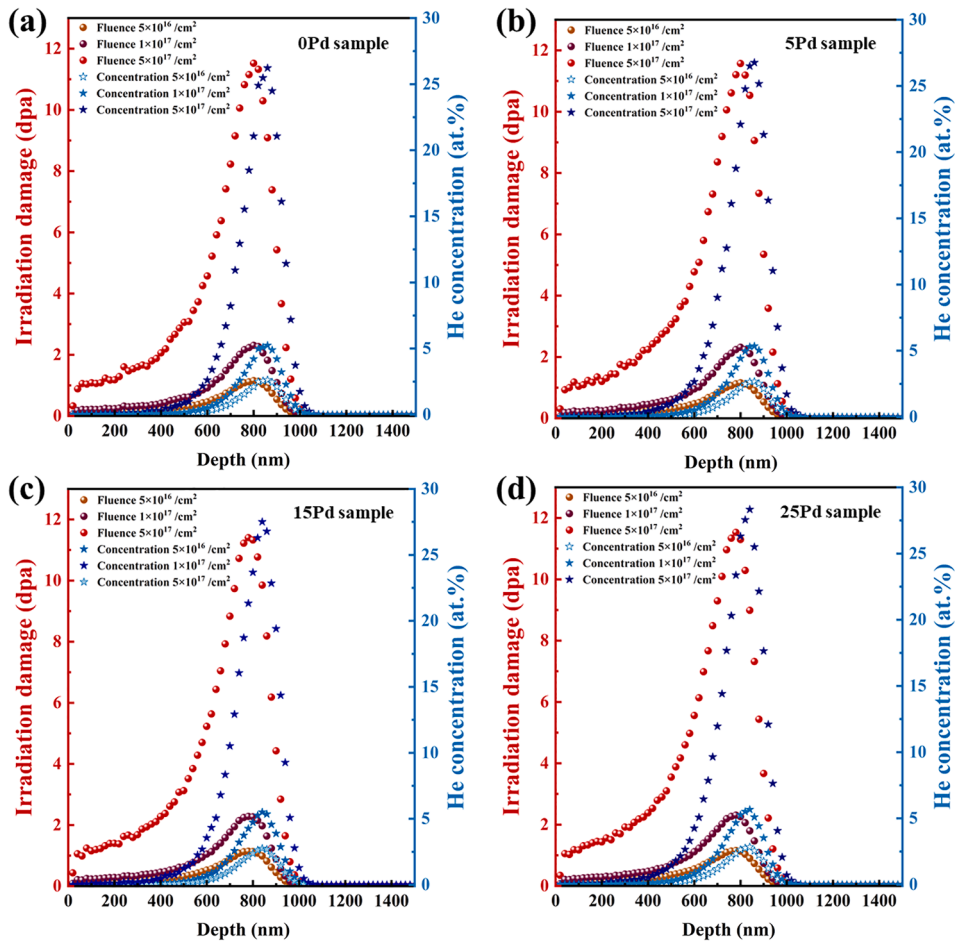


Fig. 1. SRIM calculation results of (a) 0Pd sample, (b) 5Pd sample, (c) 15Pd sample and (d) 25Pd sample.

from at least 30 test points. The maximum indentation depth and Poisson's ratio for all the tested samples were set to 2000 nm and 0.3, respectively.

### 2.3. Density functional theory (DFT) simulations

The first-principles calculations in this study were carried out by using the projected plane wave (PAW) method [22] within the Vienna Ab initio Simulation Package (VASP) code [23–25]. The  $3 \times 3 \times 3$  face-centered-cubic (FCC) structure contains 108 randomly distributed Fe, Cr, Ni, Co, and Pd atoms in normal proportion listed in Table 1, which was constructed with the assistance of the special quasi-random supercell structures (SQS) algorithm in Alloy Theoretic Automated Toolkit (ATAT) package [26] to ensure the chemical disorder in crystal structures, as Fig. 2(a–d) shown. In order to eliminate any influence of different SQS structures and guarantee reasonable computational outcomes, we created two distinct high-entropy arrangements (see Fig. S1 in Supplementary Materials). All subsequent computational results were calculated by averaging the values of both configurations.

All the systems were geometrically optimized first and then the structural properties were systematically calculated on the energy-stable structure, including vacancy formation energy and interaction energy between He interstitials and vacancies. The Perdew-Burke-Ernzerhof (PBE) functional in Generalized Gradient Approximation (GGA) [27] was set to describe the exchange correlation energy. Based on the convergence test, a plane wave cut-off energy of 500 eV and a  $2 \times 2 \times 2$  k-mesh of Monkhorst-Pack grid for the first Brillouin zone were selected, and the self-consistent convergence tolerance was set to  $1 \times 10^{-6}$  eV/atom. Considering the possible magnetic and spin polarization

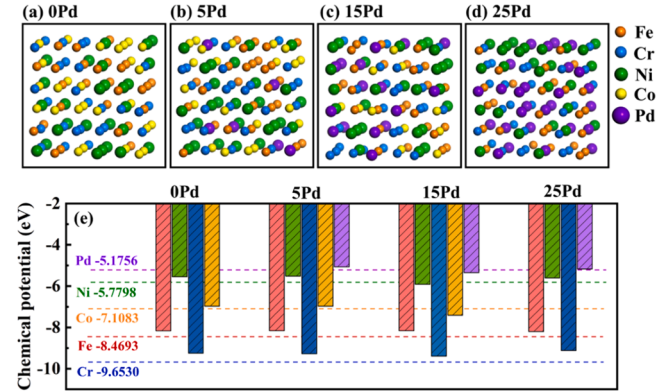


Fig. 2. Structural configurations of  $3 \times 3 \times 3$  supercell HEAs with different Pd contents. (a) 0Pd (b) 5Pd (c) 15Pd and (d) 25Pd sample. All the models contain 108 atoms. (e) The calculated chemical potential of individual element in the HEAs with different Pd contents. The dashed line represents the value of the chemical potential of the corresponding pure metal.

properties of each atom, the spin polarization in all calculations was switched on. The vacancy formation energy ( $E_V^f$ ) can be obtained by the Eq. (1) [28]:

$$E_V^f = E_V - (E_0 - \mu_p) \quad (1)$$

where  $E_V^f$  is the formation energy of a vacancy,  $p$  is the type of atom (Fe, Cr, Ni, Co, Pd), and  $\mu$  is the chemical potential of the atom. It's always

easy to get  $E_0$  and  $E_V$ , but in a high-entropy system, the chemical potential  $\mu$  of each atom cannot be obtained simply by the simple metal substance. The chemical potentials in the concentrated alloys can be determined by exchanging a randomly selected atom A with another atom B. The difference between the chemical potential of atom A,  $\mu_A$ , and that of atom B,  $\mu_B$ , could then be expressed as Eqs. (2) and (3) [29]:

$$\mu_A - \mu_B = E_{A \rightarrow B} - E \quad (2)$$

$$\mu_B - \mu_A = E_{B \rightarrow A} - E \quad (3)$$

where  $E_{A \rightarrow B}$  is the total energy of the alloy with one A atom substituted by B, and  $E$  is the total energy of the base model. The difference in reference chemical potential in an alloy can then be obtained as Eq. (4):

$$\mu_A^Z - \mu_B^Z = \frac{1}{2} (\Delta\mu_{B \rightarrow A} - \Delta\mu_{A \rightarrow B}) \quad (4)$$

where  $\Delta\mu_{A \rightarrow B}$  is the average of the “A substituted by B” substitution energies and  $\mu_A^Z$  is the chemical potential of A in alloy Z. For quaternary and quinary alloys, three independent equations out of six and four independent equations out of ten, respectively, are used to obtain results. The total energy of the system,  $E$ , should also be considered. As the calculations are performed at constant volume, neglecting all entropic contributions gives  $E$  as Eq. (5) [28]:

$$E = \sum_X N_A \mu_X^Z \quad (5)$$

where  $N_A$  is the number of X atoms in a perfect lattice and  $\mu_X^Z$  is the chemical potential of the A atom in alloy Z. The calculated chemical potential of individual element in the HEAs with different Pd contents in this study and their comparison with the chemical potential of pure metals can be found in Fig. 2(e).

The interaction energy ( $\Delta E_{He,V}$ ) between an implanted He interstitial and a vacancy can be defined as the following Eq. (6) [29]:

$$\Delta E_{He,V} = (E_0 + E_{He+V}) - (E_V + E_{He}) \quad (6)$$

where  $E_0$  represents the total energy of supercells for the perfect crystal lattice,  $E_{He+V}$  is the energy of the system with a He atom occupying a vacancy site,  $E_V$  and  $E_{He}$  are the energy of system only containing an independent vacancy or He interstitial, respectively. In order to ensure the rationality of the calculation results, all the calculations for the vacancy and the interstitial were repeated more than 10 times at different sites.

In addition, the migration energies of the interstitials in the HEAs with different Pd contents were calculated by directly optimizing saddle-point configurations [18,30], which were determined by using the

quasi-Newton method with direct inversion in the iterative subspace algorithm [31]. The interstitial migration energy ( $E_i^m$ ) can be obtained from the Eq. (7).

$$E_i^m = E_s - E_d \quad (7)$$

where  $E_s$  and  $E_d$  are the energy of the transition state and the final state of the interstitial corresponding to the Fig. S2 in *Supplementary Materials*.

### 3. Results

#### 3.1. Microstructures of the pristine HEAs with different Pd contents

Fig. 3(a) shows the XRD patterns from the pristine 0Pd, 5Pd, 15Pd and 25Pd samples, which proved that all the HEAs in this study were single phase with FCC structure. It can be found that only  $\gamma(200)$  diffraction peaks were detected in the XRD tests of all samples in this study, which may be attributed to the single crystal orientation within the X-ray detection depth caused by the coarse grain size. The Bragg angle of  $\gamma(200)$  diffraction peak of each sample decreased with the increase in Pd content, as shown in Fig. 2(b), and the lattice constant calculated from the XRD data almost linearly increased with increasing Pd content (the linear slope is about  $0.005 \text{ \AA}/\text{at.\%}$ ). The increase of the lattice constant is due to the solid solution effect of large-size atoms (the atomic radius of Co is  $152 \text{ pm}$ , and that of Pd is  $169 \text{ pm}$ ), and the specific calculated lattice constants of the HEAs with different Pd contents can be found in Table 2.

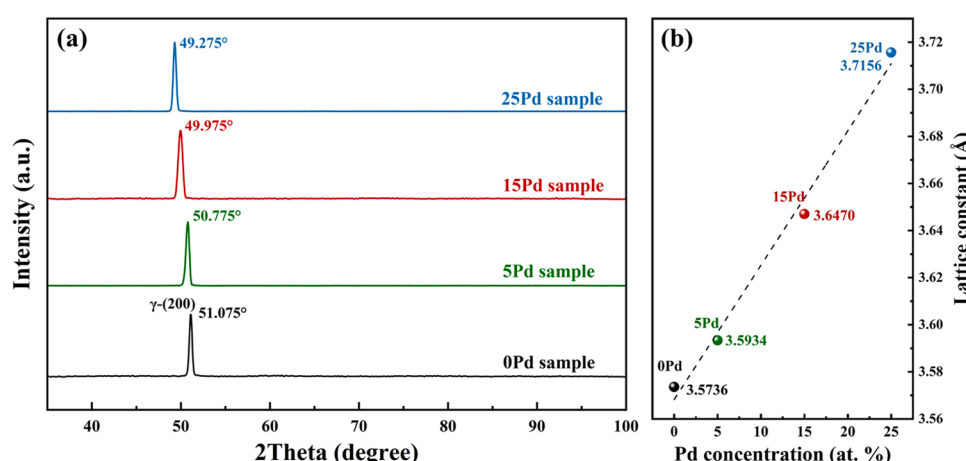
In addition, a comparison between the lattice constants determined from XRD data and those obtained from DFT calculations can also be seen in Table 2. The results show that the deviations of the lattice constants obtained by the two methods are within  $0.17 \%$ , which confirms the correctness and rationality of the supercell models with different Pd contents used for the DFT simulations in this study.

Fig. 4(a)-(d) present the atomic-resolution HAADF images and corresponding fast Fourier transform (FFT) patterns (insets) of the 0Pd, 5Pd, 15Pd and 25Pd HEAs with [011] zone axis parallel to the electron

**Table 2**

The lattice constants of the four samples calculated from XRD data ( $a_{XRD}$ ) and the DFT simulations ( $a_{DFT}$ ), and their deviations ( $\Delta a$  and  $\Delta a/a_{XRD}$ ).

Samples	$a_{XRD}$ ( $\text{\AA}$ )	$a_{DFT}$ ( $\text{\AA}$ )	$\Delta a$ ( $\text{\AA}$ )	Deviation ( $\Delta a/a_{XRD}$ )
0Pd	3.5736	3.5690	0.0046	0.13 %
5Pd	3.5934	3.5906	0.0028	0.08 %
15Pd	3.6470	3.6418	0.0052	0.14 %
25Pd	3.7156	3.7094	0.0062	0.17 %



**Fig. 3.** (a) XRD patterns from pristine 0Pd, 5Pd, 15Pd and 25Pd samples. (b) Lattice constant versus Pd content determined from the XRD data.

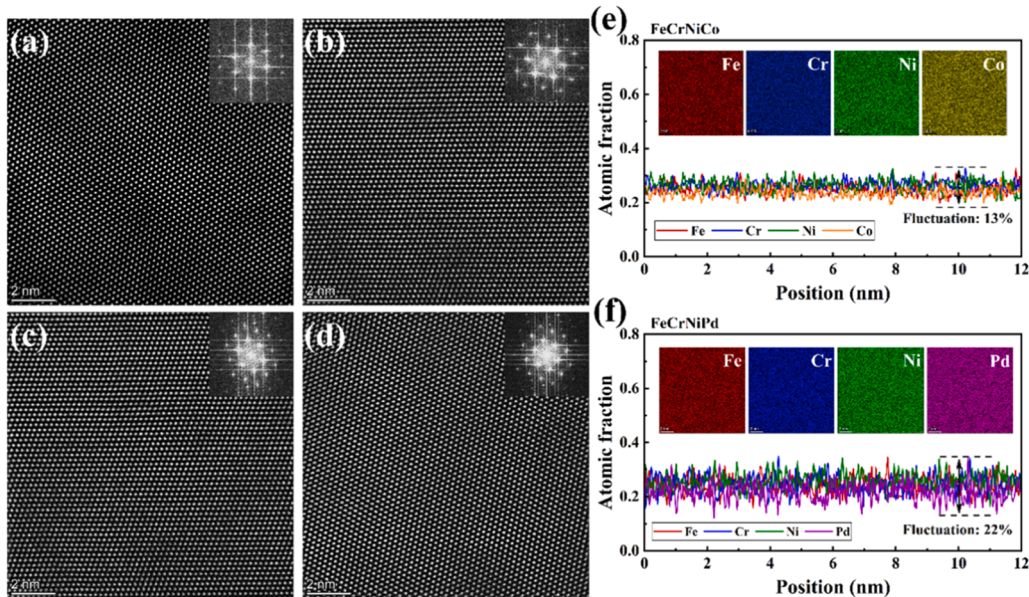


**Fig. 4.** Aberration-corrected STEM-HAADF images of (a) 0Pd, (b) 5Pd, (c) 15Pd and (d) 25Pd sample taken with [011] zone axis; insets in (a)–(d) are corresponding FFT patterns of the images. EDS mapping of element distributions in the (e) 0Pd and (f) 25Pd sample, and line profiles of atomic fraction of individual elements taken from the respective EDS maps; the line profiles represent the distribution of an element in the (111) plane projected along the [011] beam direction. The dashed lines in (e) and (f) represent the fluctuation range of the individual element concentrations in 0Pd and 25Pd sample, respectively.

beam, respectively, showing only the normal FCC Bragg spots. Fig. 4(e) shows the corresponding EDS mapping and line profiles of atomic fraction of individual elements of FeCrNiCo (0Pd). The detectable undulation (the maximum fluctuation is about 13 %) was observed in the atomic concentration of Fe, Cr, Ni and Co, and the peaks and valleys of each element appear periodically at a spacing of ~1 nm. Similar but different, as shown in Fig. 4(f), such chemical component fluctuations of

1 nm spacing between peaks and valleys can also be detected in FeCrNiPd (25Pd), but the fluctuation behavior of each element in 25Pd is quite different compared to that in 0Pd (similar fluctuation of each element in 0Pd). Specifically, the fluctuation of Pd (about 22 %) in 25Pd is more obvious than that of Fe, Cr and Ni, but still maintains 1 nm peak and valley spacing. These phenomena have been reported in recent studies of HEAs [12,32] and are thought to be attributable to the

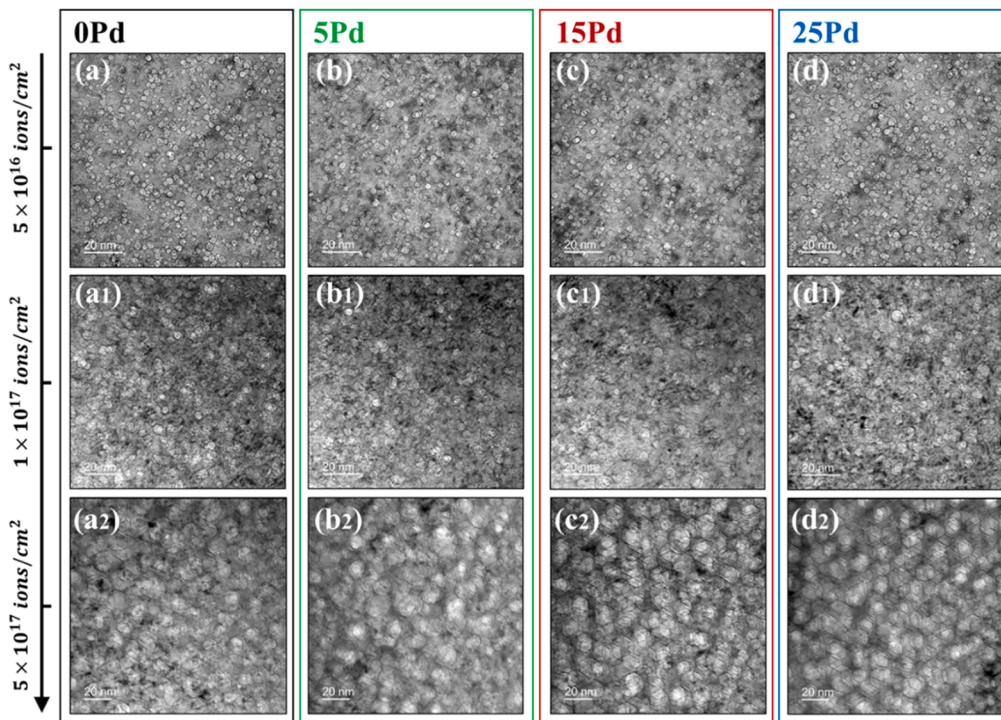


**Fig. 5.** TEM-BF images of He bubbles at peak He concentration regions in He ion-irradiated (a)–(a2) 0Pd, (b)–(b2) 5Pd, (c)–(c2) 15Pd and (d)–(d2) 25Pd samples. Among them, the images correspond to the samples irradiated to the fluence of (a)–(d)  $5 \times 10^{16} \text{ cm}^{-2}$ , (a1)–(d1)  $1 \times 10^{17} \text{ cm}^{-2}$ , and (a2)–(d2)  $5 \times 10^{17} \text{ cm}^{-2}$ . All images were acquired at the condition away from the [011] to a high-order zone axis and were taken at under-focus  $\sim 0.5 \mu\text{m}$ .

chemical short-range order (CSRO) in HEAs (or medium-entropy alloys, MEAs) [33–35]. It can be found that the fluctuation degree of all elements in 25Pd is larger than that in 0Pd, thus, indicating that the alloying of Pd contributes to increasing the extent of CSRO in FeCrNiCo HEAs. This finding is consistent with Ding's report [12] and not described in detail herein.

### 3.2. Bubbles in the He ion-irradiated HEAs with different Pd contents

The increased chemical heterogeneities caused by the introduction of Pd in FeCrNiCo are considered to have non-negligible effects on the evolution of point defects, which can be used as a feasible way to regulate the irradiation resistance of HEAs [32]. To evaluate the microstructure evolution of the Pd-containing HEAs with the proven CSRO under He ion irradiation, we performed 400 keV He ion irradiation at 723 K to several fluences ( $5 \times 10^{16}$  ions/cm<sup>2</sup>,  $1 \times 10^{17}$  ions/cm<sup>2</sup>, and  $5 \times 10^{17}$  ions/cm<sup>2</sup>). For illustrative purposes, the three He ion irradiation doses in this study will be referred to as low dose, medium dose and high dose, respectively. Fig. 5 presents the cross-sectional TEM-BF images (the images were taken at under-focus  $\sim 0.5$  μm to reveal the presence of He bubbles, thus, the He bubbles appear as bright contrast) of the HEAs with different Pd contents irradiated to the three doses, and all images were acquired from the peak He concentration regions (depth of  $\sim 800$  nm).

He bubbles are present in all the irradiated samples and at all irradiation doses in this study, apparently, and the higher the dose, the larger the bubble diameter. At low dose conditions, as shown in Fig. 5 (a)–(d), the bubbles exhibit as individual spheres with relatively uniform diameters of 2–3 nm. As the dose increases, the He bubble gradually changes from the standard-sphere shape (low dose) to an ellipsoid shape (medium dose, see Fig. 5(a1)–(d1)) then to a nearly hexagon shape similar to that of irradiation-induced voids [36] (high dose, see Fig. 5 (a2)–(d2)), which is largely determined by the ratio of He to vacancy in bubbles, or the pressure/He density within the bubbles [37]. In general, hexagonal bubbles indicate low internal pressure (or He density) and spherical bubbles indicate high internal pressure (or He density), which can be explained by Laplace-Young's law [38], that is, the He density within an individual bubble decreases with increasing the diameter of the bubble. In addition, the overlap of bubbles was observed at medium and high dose conditions, and the differences in bubble diameters within the same sample increased significantly. This is due to the combination of small bubbles to large-sized bubbles. The surviving small-sized bubbles coexist with the large ones, causing the differential expansion between the bubble diameters within the same sample.

To quantify the He bubbles of the four HEAs with different Pd contents under several irradiation doses, the diameters and number densities of the bubbles at the depth range of 700–900 nm in all irradiated

HEAs were carefully measured and counted, and the statistical results were obtained from at least 10 images, covering an area of  $\sim 0.07$  μm<sup>2</sup>. Fig. 6 shows the statistical results of average bubble diameter and number density of bubbles in the four HEAs to the three irradiation fluences, and both diameter and density increased significantly with the increase of irradiation fluence. By comparing the HEAs with different Pd content, it can be found that the diameter of the bubble is positively correlated with the Pd content, and the trend becomes more and more significant with the increase of dose. Similarly, bubble density also increased with increasing Pd content, but this phenomenon was more prominent at low dose.

In addition, Fig. 7 presents the atomic-resolution STEM-HAADF images of the bubbles observed in 0Pd and 25Pd samples after irradiation to a fluence of  $5 \times 10^{16}$  ions/cm<sup>2</sup> under the two imaging conditions (Z=[001] and Z=[011]), along with corresponding EDS maps of element distributions. Fig. 7(a) and (c) show the morphology and elemental distribution of the bubbles in the 0Pd sample, respectively, indicating that the bubbles are surrounded by a detectable Ni enrichment. This is evidenced by the fact that the Ni concentration within approximately 1 nm surrounding the bubbles is notably higher than that of Fe, Cr, and Co. Specifically, the Ni concentration around the bubbles could surpass 40 at.%, whereas Fe, Cr, and Co fluctuate around  $\sim 25$  at.% (with fluctuation ranges similar to those in the matrix).

However, as demonstrated in Fig. 7(b) and (d), it is interesting to note that the Ni enrichment surrounding a bubble is absent in the 25Pd sample, despite the identical irradiation conditions and Ni contents of both the 0Pd and 25Pd samples (25 at.% Ni in both samples). The EDS data of the 25Pd sample shows that the individual elements around the bubbles exhibit a fluctuating behavior that is essentially consistent with the matrix in both Z=[001] and Z=[011] conditions. It is worth noting that the variability in chemical fluctuation behavior poses a challenge for EDS data to provide a direct quantitative measurement of Ni segregation around bubbles. Chemical fluctuations are intrinsic to HEAs, suggesting that they are prevalent both in the matrix and around the bubbles, making EDS-detected Ni enrichment a definite occurrence. Moreover, the characterization results of several additional bubbles confirm the Ni enrichment in 0Pd but its absence in 25Pd. Further details are available in Figs. S3 and S4 of *Supplementary Materials*.

### 3.3. Dislocation loops in the He ion-irradiated HEAs with different Pd contents

Dislocation loop is another typical microscopic defect introduced by He ion irradiation for metals [1]. To systematically evaluate the irradiation resistance of the Pd-containing HEAs in this study, the irradiation-induced dislocation loops in the HEAs with different Pd contents at the three irradiation doses were characterized and counted.

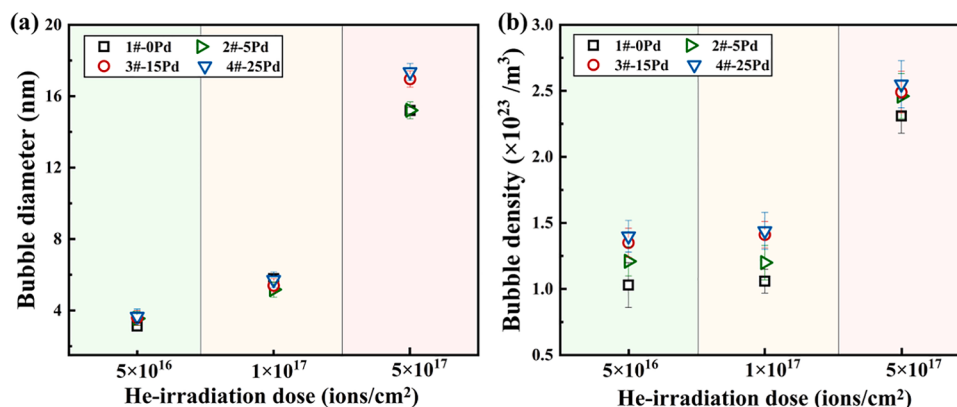
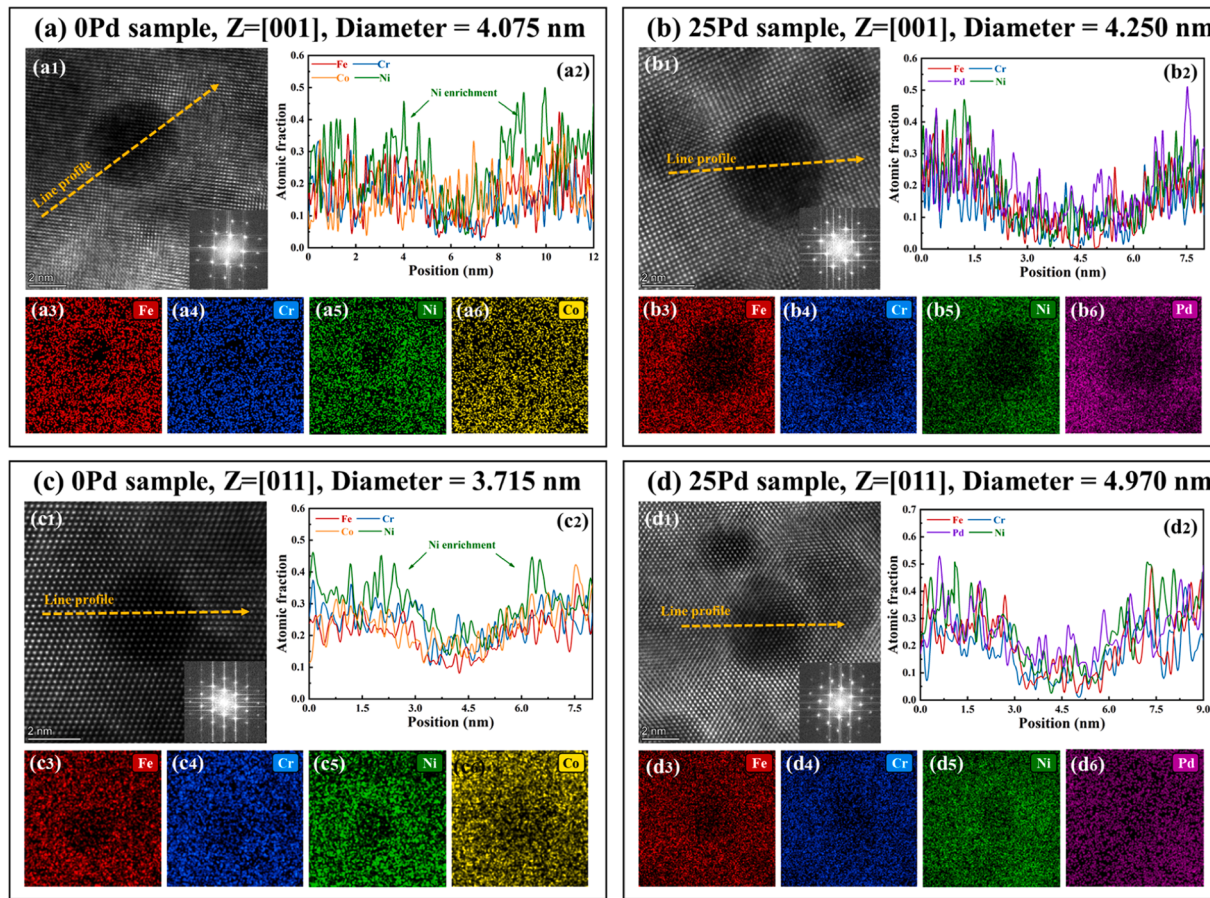


Fig. 6. Statistical results of (a) average bubble diameter and (b) bubble number density. The measurement error of bubble diameter and density is due to the illegibility of overlapping bubbles and the uncertainty of the sample thickness.



**Fig. 7.** Atomic-resolution STEM-HAADF images of the He bubbles in (a1) and (c1) 0Pd, (b1) and (d1) 25Pd sample after He-irradiation fluence to  $5 \times 10^{16}$  ions/cm<sup>2</sup>. The images were taken with the [001] and [011] zone axis, respectively, and the near-circular dark contrast regions represent He bubbles. EDS mapping of element distributions in the (a3)–(a6) and (c3)–(c6) 0Pd, (b3)–(b6) and (d3)–(d6) 25Pd sample, and (a2)–(d2) are line profiles of atomic fraction of individual elements taken from the respective EDS maps; the positions of the corresponding scan lines are respectively indicated by orange arrows in (a1)–(d1). (For interpretation of the references to colour in this figure legend, the reader is referred to the web version of this article.)

**Fig. 8(a)–(d)** show typical STEM-BF images of the dislocation loops at peak damage regions (depth of ~700 nm) in 0Pd, 5Pd, 15Pd, and 25Pd samples after He-irradiation. Vary from the heavy-ion irradiation conditions that tend to produce a large number of faulted loops and stacking fault tetrahedra (SFT) in HEAs [39–41], the  $1/2<110>$  perfect loops are considered to be the predominant dislocation loop type at low and medium doses based on observations in this study, and the dislocation loops and He bubbles overlap to form complex dislocation tangles at high dose.

**Fig. 8(e) and (f)** show statistical results for the average loop size and loop density of the samples after several irradiation doses. It can be found that the average loop size decreases with the increase of Pd content under the three irradiation doses, and increases with the increase of irradiation dose. Under the same irradiation conditions, the average sizes of the dislocation loops are inversely proportional to the Pd content in HEAs, which is the most obvious at low irradiation dose. This phenomenon suggests that Pd alloying can inhibit the growth of dislocation loops (especially at low irradiation dose), which is consistent with previous reports [17]. In addition, the density of dislocation loops increases with the increase of Pd content, which is the most obvious at high dose. Specifically, the density of dislocation loops in 25Pd was more than twice that of the 0Pd at high doses, but only about 1.6 times that of the 0Pd at low doses. Overall, it is suggested that Pd alloying contributes to inhibiting the evolution of dislocation loops in HEAs, which is manifested by suppressing the growth of loops at low doses and preventing the movement of loops from evolving into large defects such as dislocation networks at high doses.

However, the formation and growth of dislocation loops produced by He ion irradiation not only need to consider the evolution of irradiation-induced point defects (including self-interstitials, vacancies, and their clusters), but also can be greatly affected by the behaviors of He bubbles. The possible interactions between dislocation loops and He bubbles in the HEAs with different Pd contents are discussed in Chapter 4.2.

### 3.4. Irradiation-induced hardening in the HEAs with different Pd contents

High-density defects introduced by irradiation can act as obstacles to dislocation motion and result in the hardening of the irradiated materials [42,43]. Therefore, the determination of hardening can be used as one of the important bases to evaluate the irradiation resistance of the materials. **Fig. 9(a)–(d)** show the average hardness ( $H$ ) versus depth ( $h$ ) of 0Pd, 5Pd, 15Pd, and 25Pd samples before and after irradiation to fluences of  $5 \times 10^{16}$  cm<sup>-2</sup>,  $1 \times 10^{17}$  cm<sup>-2</sup>, and  $5 \times 10^{17}$  cm<sup>-2</sup>, respectively. The hardness of the pristine samples shows the smooth curves that gradually decreased with the increase of indentation depth, while the curves of irradiated samples exhibit bulging in the depth range of 50–300 nm (the regions highlighted by red circles in **Fig. 9**), and these bulges become more significant with the increase of irradiation dose. Among them, the hardness decrease with increasing indentation depth is attributed to the indentation size effect (ISE) [44], and the bulges on the curves of irradiated samples are due to the combined effects of the concentrated distribution of irradiation defects (depth of ~800 nm) and the soft substrate effect (SSE) [45].

In order to exclude the interference of ISE and to obtain the reliable

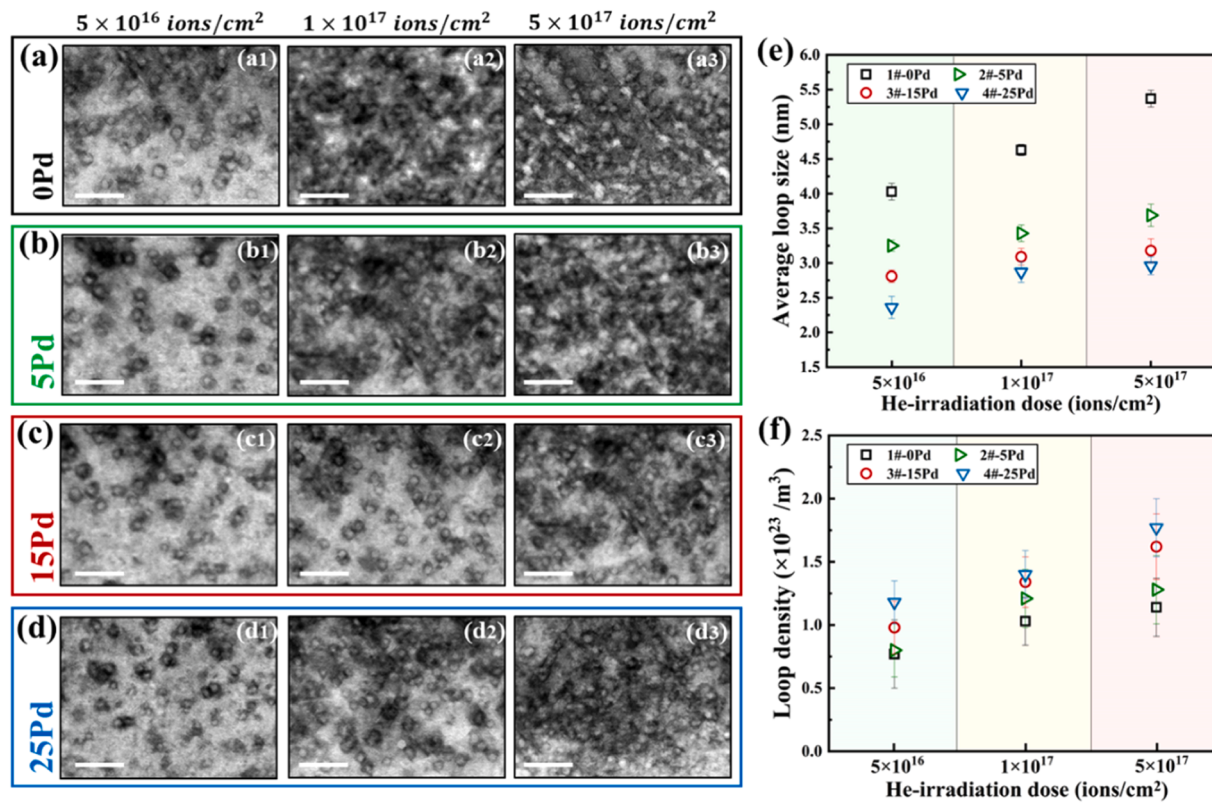


**Fig. 8.** STEM-BF images of dislocation loops at peak damage regions in (a) 0Pd, (b) 5Pd, (c) 15Pd and (d) 25Pd sample irradiated to the fluences of (a1)–(d1)  $5 \times 10^{16}$  cm<sup>-2</sup>, (a2)–(d2)  $1 \times 10^{17}$  cm<sup>-2</sup>, and (a3)–(d3)  $5 \times 10^{17}$  cm<sup>-2</sup>. All the images were taken at the [011] zone axis, and the scale bars in all the images represent 20 nm. (e) and (f) are statistical results for the average loop size (in nm) and loop density (in m<sup>-3</sup>) for all the irradiated samples.

hardness of the irradiation-affected zones, Kasada et al. proposed a method based on the Nix-Gao model for extracting the real hardness ( $H_0$ ) from the original curves of hardness versus depth [46,47], which can be described by the Eq. (8).

$$H = H_0 \sqrt{1 + \frac{h^*}{h}} \quad (8)$$

where  $H_0$  is the real hardness at infinite depth,  $h$  represents the indentation depth, and  $h^*$  denotes the characteristic length that depends on the indenter shape and the measured material. According to the ISE described in Eq. (8), the raw data were plotted as the square of hardness ( $H^2$ ) and the reciprocal of the indentation depth ( $1/h$ ), as shown in Fig. 10(a)–(d), and the intercepts after curve fitting are the square of the real hardness.

It can be seen that the curves fitted from the data of the pristine samples are unilinear, while those of the irradiated samples exhibit typical bilinear patterns with evident inflection points ( $h_c$ ) at a depth range of 200–213 nm. These results are due to the uniform hardness in pristine samples and SSE in irradiated samples, respectively. Based on a previous report [48], the hardness data can be affected by the regions with 4–10 times the indentation depth, implying that the inflection points of the bilinear curves indicate the depth at which SSE occurs. In this study, the depth of the inflection point (~200 nm) is around 1/5 of the irradiation damage layer (~1000 nm), indicating that the Berkovich indenter could reflect the hardness of the indent extending down to ~5 times the contact depth in the FCC HEAs, which is consistent with previous findings [45]. However, in the present study, the hardening behavior under He ion irradiation is a complex result of the simultaneous effects of dislocation loops and bubbles, and the contribution on hardening of dislocation loops and bubbles can be calculated independently (see Chapter 4.3 for details). In addition, Fig. 10(e) shows the three hardening stages corresponding to the three irradiation doses in

this study, indicating that there are three distinct stages of hardening in response to irradiation dose (the rapid rising stage, the inflection point stage and the stable stage, respectively). Fig. 10(f)–(h) show the hardening rate of the samples after irradiation to the fluences of  $5 \times 10^{16}$  cm<sup>-2</sup>,  $1 \times 10^{17}$  cm<sup>-2</sup>, and  $5 \times 10^{17}$  cm<sup>-2</sup>, corresponding to the three stages indicated in Fig. 10(e). The results showed that the hardening rate of the samples decreased with the increase of Pd content at low dose, and the same trend was still observed at medium dose (but the hardening rate of 15Pd and 25Pd was close). Moreover, it is interesting to note that the hardening rate exhibited a completely opposite trend at high dose to that at low dose, suggesting that the hardening rate was no longer inhibited by the increase in Pd content at high dose. These phenomena are due to different hardening mechanisms (contribution ratios of dislocation loops and bubbles) caused by different He concentrations (irradiation doses), which are discussed in Chapter 4.3.

## 4. Discussion

### 4.1. The role of Pd content on the evolution of He bubbles

The radius of He atom (31 pm) is significantly smaller than that of common interstitial solid solution atoms in metallic materials (67 pm for C atom, 56 pm for N atom), which means that He atoms have a strong tendency to migrate and evolve in He ion-irradiated metallic materials. The evolution of He bubbles can be divided into two stages in this study: formation and growth. The formation and growth of bubbles is a dynamic process that is closely related to the introduction of vacancies and the binding of implanted He atoms to these vacancies, apparently, which can be described by the vacancy formation energy ( $E_V^f$ ) and the interaction energy ( $\Delta E_{He,V}$ ) between the He atom and vacancy in the HEAs with different Pd contents. Fig. 11(a)–(e) show the  $E_V^f$  of the four HEAs in this study calculated by DFT simulations, which clearly indicates a rule:

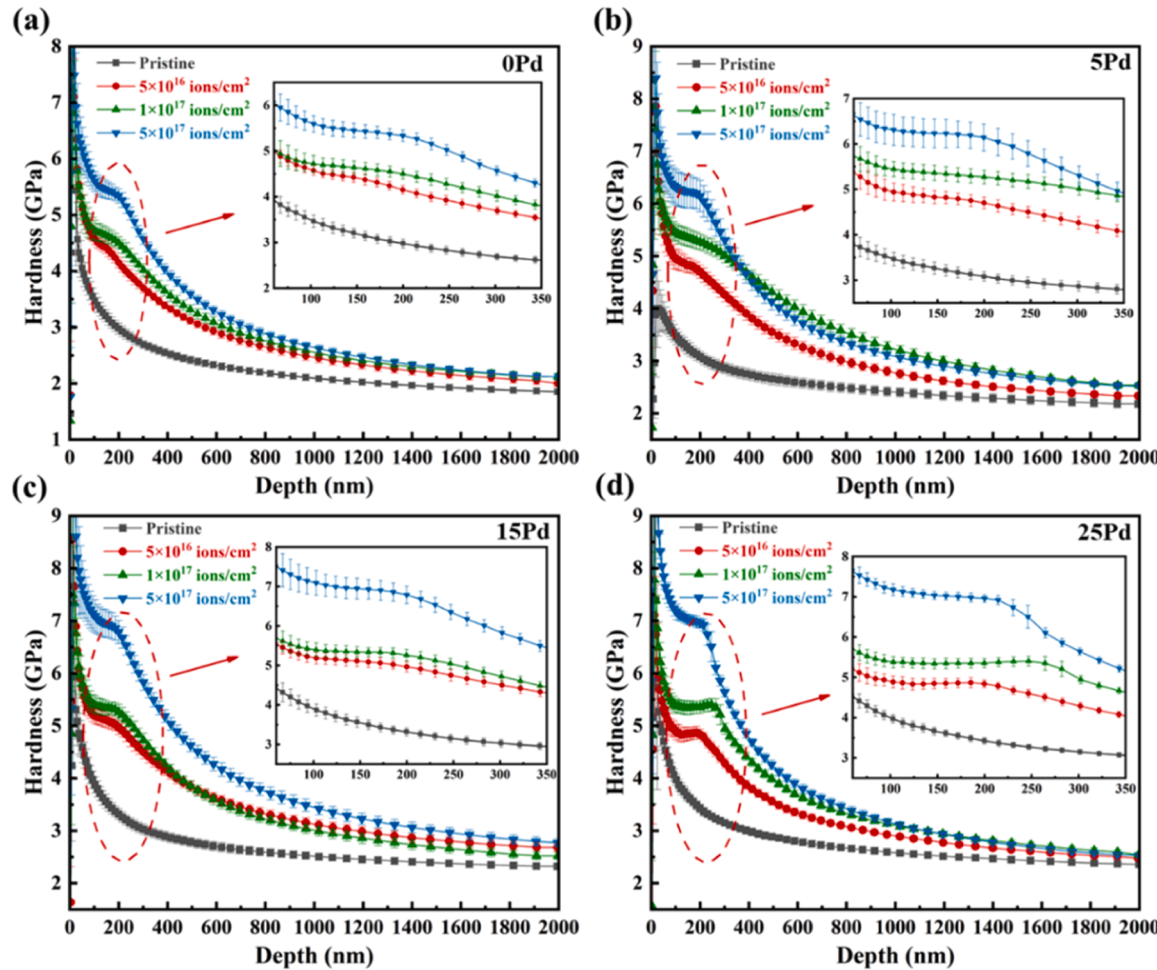


**Fig. 9.** Average nanoindentation hardness versus the indentation depth of (a) 0Pd, (b) 5Pd, (c) 15Pd, and (d) 25Pd sample before and after three doses of He-irradiations ( $5 \times 10^{16} \text{ cm}^{-2}$ ,  $1 \times 10^{17} \text{ cm}^{-2}$ , and  $5 \times 10^{17} \text{ cm}^{-2}$ ). Insets are the zoomed-in images of the corresponding curves at depth of 30 nm to 350 nm (positions circled by red dotted lines).

with the increase of Pd content (accompanied by the decrease of Co content) in the HEAs, the  $E_V^f$  corresponding to all elements decreases linearly. This finding can be corroborated by a recent report that doping alloying elements (such as Al, Cu, Pd, and Ti) can decrease vacancy formation energies while enhancing migration energies [18]. In addition, Fig. 11(f) shows the linear slope of the linear decrease of  $E_V^f$  of each element with the increase of Pd content. The results show that the  $E_V^f$  of Fe, Cr and Ni with constant content in the HEAs has almost the same response to Pd alloying: 1 at.% Pd alloying (accompanied by the replacement of Co) reduces  $E_V^f$  of 0.038eV, which may provide theoretical guidance for the design of Pd-containing HEAs.

The reduced  $E_V^f$  in Pd-containing HEAs, on the one hand, can lead to a large concentration of unsteady vacancies under the same irradiation conditions, which means that more movable vacancies are available for bubble formation. On the other hand, these irradiation-induced vacancies can trap the implanted He atoms to form the He-Vacancy complexes and act as the nucleation sites, promoting the formation of the He bubbles. Specifically, Fig. 12 shows the  $\Delta E_{He,V}$  between the He interstitials and vacancies calculated by DFT, suggesting that the alloying of Pd inevitably leads to a decrease in the  $\Delta E_{He,V}$  between Fe, Cr, Ni, Co vacancies and He interstitials (the more negative  $\Delta E_{He,V}$  corresponds to the more inclined to the combination of He interstitials and vacancies [29]). This result indicates that the vacancies in the Pd-containing HEAs have a stronger attraction to the He interstitials, which means that the formation of He bubbles is promoted. Furthermore, the growth of He

bubbles is thought to be achieved primarily through the migration/coalescence of small-sized bubbles and the accumulation of vacancies/He atoms in large-sized bubbles [49]. As mentioned above, the stronger attraction of the vacancy to He atoms could accelerate the accumulation process and promote the coarsening of He bubbles in Pd-containing HEAs. Therefore, it can be concluded that Pd alloying (accompanied by the replacement of Co) in FeCrNiCo HEAs would promote the formation and growth of He bubbles due to the reduction of  $E_V^f$  and  $\Delta E_{He,V}$ , which is also verified by the statistical results of He bubbles in this study.

Moreover, the Ni enrichment at the periphery of the bubble was observed in 0Pd sample. Chen et al. [39] showed that the depletion/enrichment of individual elements around the defect sinks in irradiated HEAs is closely related to their volume size factor (VSF) and migration energy ( $E_i^m$ ). Helium bubbles or voids, apparently, belong to a kind of defect sink, and the elemental segregation around them after irradiation can be evaluated and explained by the VSF and  $E_i^m$  of individual elements. The VSF is defined as the fractional molar volume change per unit change in concentration of solute, and in general an increasing VSF corresponds to a decrease in enrichment and an increase in depletion. King [50] reported the order of VSF of the elements in Ni matrix as Mn > Fe > Cr > Co > Ni (specifically, the VSF of Ni is 0 %, Co is 1.76 %, Cr is 10.34 %, Fe is 10.57 %, and Mn is 23.2 %), which suggests that Ni element has a greater tendency to enrich at the periphery of bubbles compared to Fe, Cr, and Co elements, and this is consistent with our findings in FeCrNiCo (0Pd) sample. Similar enrichment of Ni in the

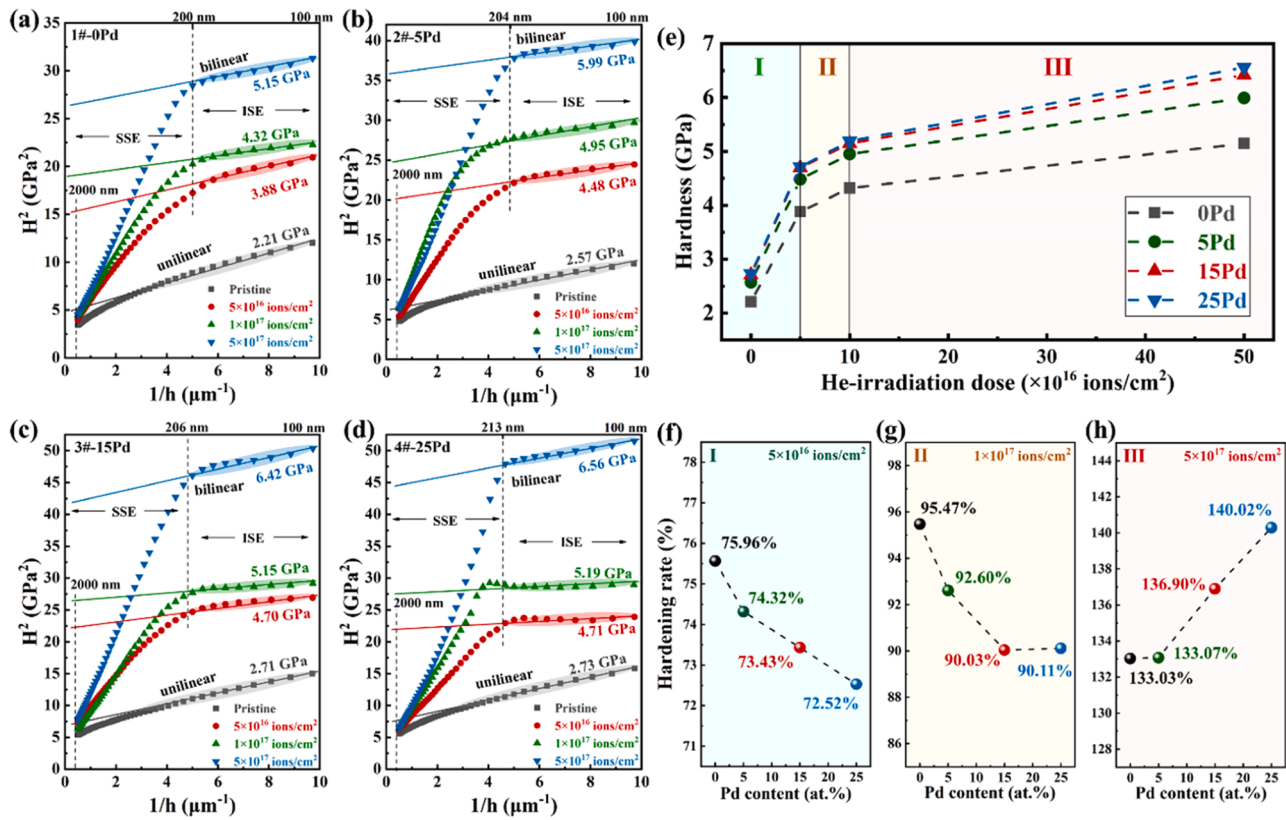


**Fig. 10.** The curves of  $H^2$ – $1/h$  for the average nanoindentation hardness of (a) 0Pd, (b) 5Pd, (c) 15Pd and (d) 25Pd sample before and after three doses of He-irradiations ( $5 \times 10^{16}$  cm<sup>-2</sup>,  $1 \times 10^{17}$  cm<sup>-2</sup>, and  $5 \times 10^{17}$  cm<sup>-2</sup>). (e) Comparison of nanohardness of all the samples before and after the irradiations, and stage I, II and III respectively represent the rapid rising stage, the inflection point stage and the stable stage. The relationship between hardening rate and Pd content under the He-irradiation doses of (f)  $5 \times 10^{16}$  cm<sup>-2</sup>, (g)  $1 \times 10^{17}$  cm<sup>-2</sup>, and (h)  $5 \times 10^{17}$  cm<sup>-2</sup>.

vicinity of defect sinks (dislocation loops, free surfaces) has been reported in previous studies [39,51,52].

However, in the present study, it is found that the Ni enrichment at the periphery of bubbles was unexpectedly absent in the Pd-containing HEAs, which may be attributed to the significant change in the migration energy of the interstitials in Pd-containing HEAs compared to that in the 0Pd sample. It is worth mentioning that the alloying of Pd clearly does not change the VSF of Ni itself which is the smallest of all the elements in Pd-containing HEAs. The calculated interstitial migration energies ( $E_i^m$ ) of individual elements in the four HEAs are displayed in Fig. 13(a)–(e), indicating that the interstitial migration energies of individual elements increase significantly and linearly with increasing Pd content. Furthermore, as shown in Fig. 13(f) and (g), it can be found that the migration energy of Ni is the smallest among all the elements in each HEA with the same Pd content, and the gap in the normalized migration energy of individual element compared to Ni decreases significantly with Pd alloying. These results can be rationalized to explain the Ni enrichment around the bubbles detected in 0Pd sample but absent in 25Pd sample. On the one hand, the relatively low interstitial migration energy in 0Pd allows all kinds of interstitials to migrate toward the bubbles, and because Ni has the lowest migration energy, the detectable Ni enrichment around the bubble is eventually formed. However, the Pd alloying significantly increases the migration energies of all elements, and the tendency of interstitials to migrate toward the bubbles is suppressed. On the other hand, the gaps between the migration energies of Ni and other elements decrease with increasing Pd content, which implies that the migration behavior of Ni interstitials and other interstitials around bubbles tends to converge.

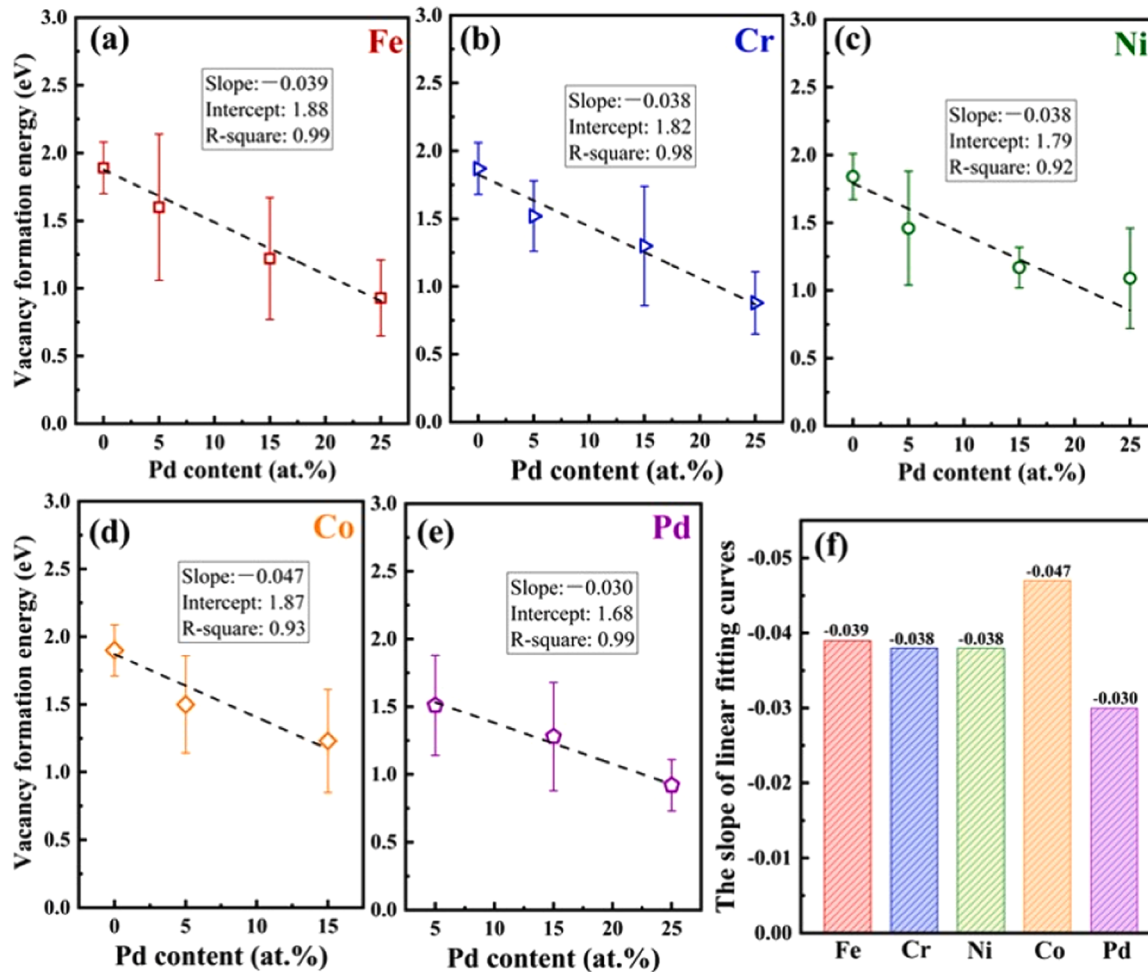
In addition, with the alloying of Pd, the  $\Delta E_{He,V}$  of the Ni vacancy is no longer as far ahead as in the 0Pd sample, and it is the reduction of the difference in  $\Delta E_{He,V}$  between Ni vacancy and others that leads to the

absence of Ni enrichment around the bubble in the 25Pd sample. The other plausible explanation takes into account the chemically-biased diffusion associated with the sluggish diffusion effects in HEAs. Zhang et al. [53] suggested that the segregations near defect sinks achieved by chemically-biased diffusion via irradiation-induced point defects would effectively inhibit void growth and convert void nuclei into Ni-rich precipitates in Ni-based concentrated solid-solution alloys. Indeed, the enrichment of Ni around bubbles was observed in 0Pd with a more significant inhibition effect on bubble coarsening, while the Ni segregation was absent in 25Pd with correspondingly larger bubble diameters. These findings indicate that the segregation behavior around He bubbles can be significantly influenced by the changes of elements in HEAs via regulating the VSF,  $E_i^m$ , and  $\Delta E_{He,V}$  between the vacancies and He interstitials.

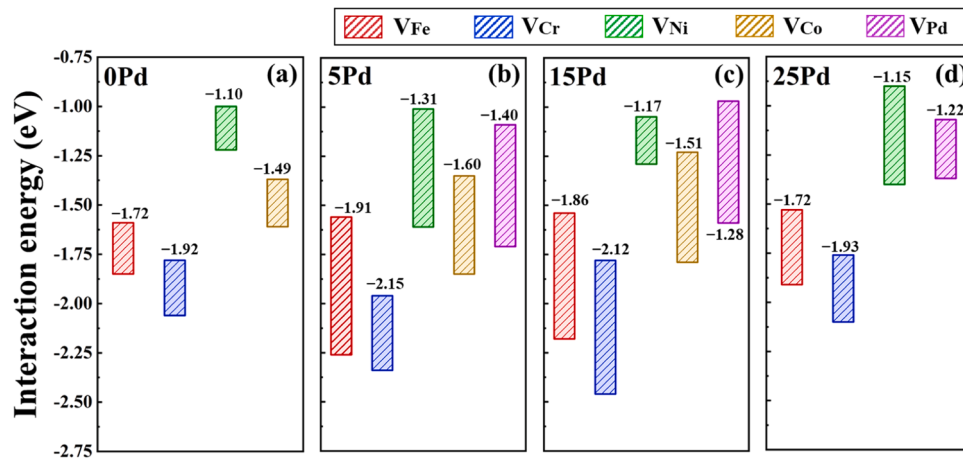
#### 4.2. The effects of bubbles on dislocation loops in Pd-containing HEAs

He ion irradiation on metallic materials not only introduces He atoms into the matrix, but also produces primary point defects including interstitials and vacancies. These point defects evolve and eventually form dislocation loops [54]. Most microscopic studies on He bubble itself, while the studies on the effect of He on dislocation loops are limited. The interactions between He bubbles and irradiation-induced defects may play a dominant role in the evolution of dislocation loops in the materials exposed to He ion irradiation, which needs to be studied and explained in the HEAs with different Pd contents.

He bubbles promote the formation and evolution of dislocation loops. For one thing, the loop punching mechanism [55] is considered to be the important incentive for the formation of dislocation loops under the He ion irradiation condition in this study (low level of collision with



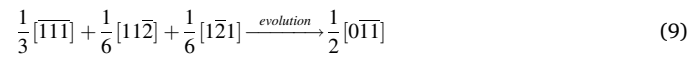
**Fig. 11.** Vacancy formation energy of individual elements in the HEAs with different Pd contents calculated by DFT: (a) Fe, (b) Cr, (c) Ni, (d) Co and (e) Pd. The ordinates of the (a)–(e) represent the vacancy formation energy (in eV). (f) is the linear coefficient of the linear variation of the vacancy formation energy of each element as the Pd content increases.



**Fig. 12.** Interaction energy ( $\Delta E_{He,V}$ ) between an implanted He interstitial and a vacancy of an individual element in (a) 0Pd, (b) 5Pd, (c) 15Pd and (d) 25Pd sample. The numerical values on the top (bottom) of each floating bar chart represent the corresponding average values of multiple DFT calculations.

high local He concentration). The process of loop punching can be described as He atoms aggregating to form small-sized He clusters accompanied by stress fields around them, and the adjacent atoms can be directly extruded out of the lattice after the pressure of the stress field is high enough. These extruded atoms tend to evolve into interstitial

dislocation loops with Burgers vector ( $b$ ) of  $1/2<110>$  to reduce the increasing strain field, which is usually done through the following reaction between several types of stacking faults (see Eq. (9)).



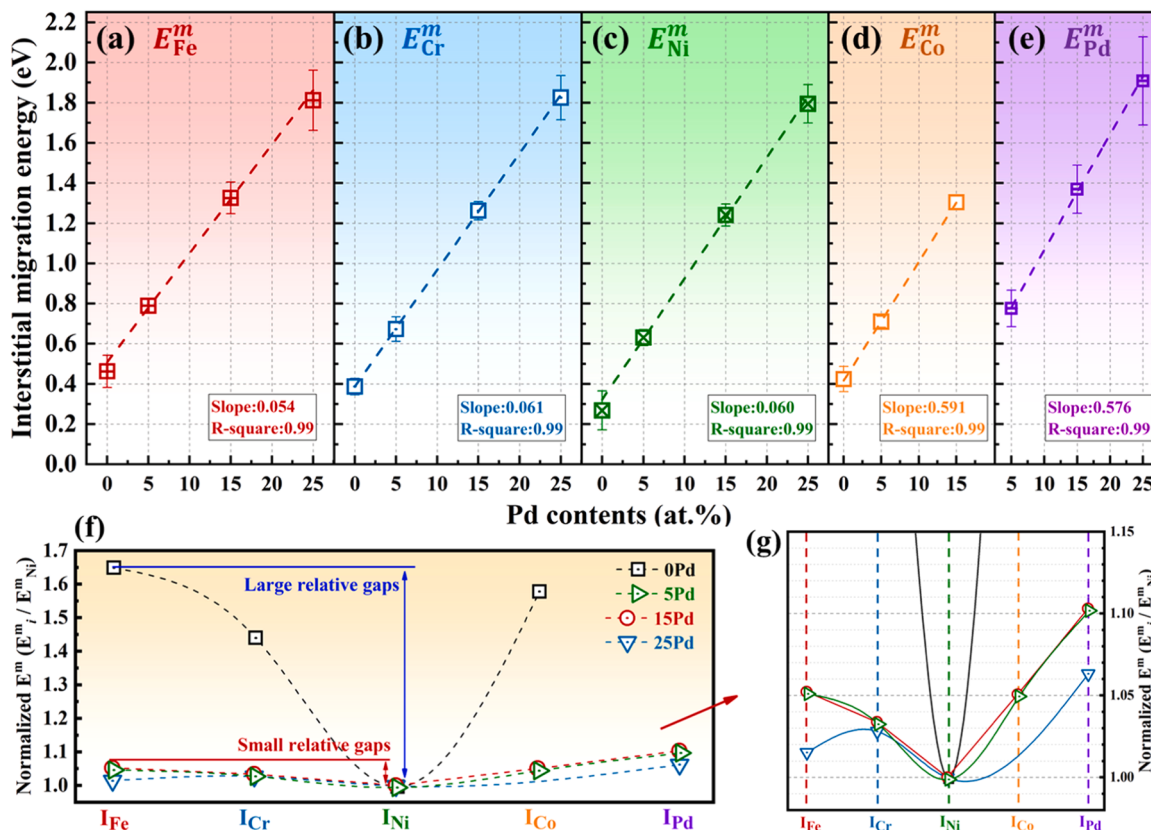


**Fig. 13.** Interstitial migration energy of individual elements in the HEAs with different Pd contents calculated by DFT: (a) Fe, (b) Cr, (c) Ni, (d) Co, and (e) Pd. (a)–(e) share the same vertical axis scale, and the horizontal coordinates indicate the Pd contents of the HEAs. (f) The normalized interstitial migration energy of individual elements based on the migration energy of Ni in the four HEAs with different Pd contents (ratio of migration energies of other elements to Ni). (g) is a localized and enlarged presentation of the data in (f).

As shown in Fig. 14(a), several dislocation loops can be observed around each individual He bubble in 25Pd sample. These dislocation loops, which are almost symmetrically distributed along the bubble, can be considered as the perfect loops with  $b=1/2<110>$  generated by the loop punching mechanism. Fig. 14(b) and (c) show TEM-BF images of the stress distortion around the bubbles taken at in-focus and under-

focus conditions, respectively, and obvious strip folds can be found in the areas marked by red arrows. The corresponding FFT patterns show that no structures other than the matrix FCC with  $Z=[011]$  were detected, confirming that these stress distortions were caused by implanted He. These phenomena indicate that He bubbles can produce non-negligible stress fields in the matrix and generate a large number of

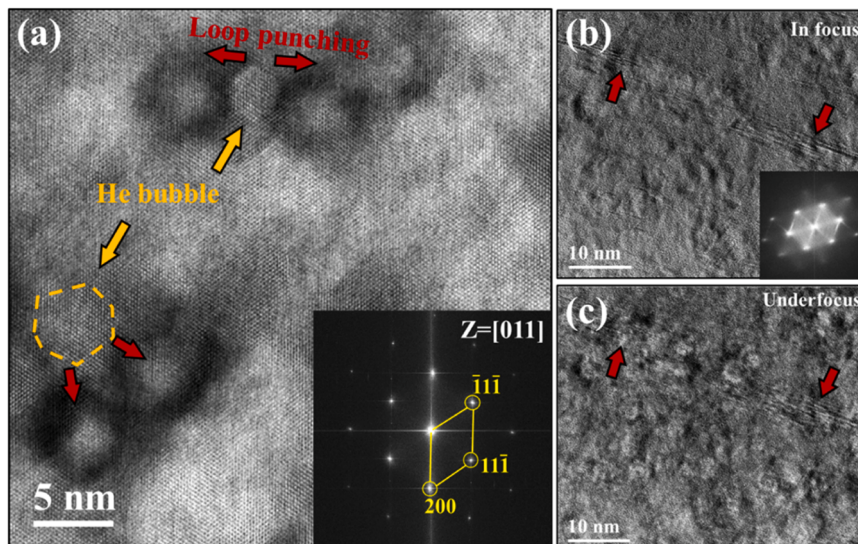


**Fig. 14.** (a) STEM-BF image of typical loop punching mechanism in 25Pd sample after He ion irradiation to the fluence of  $5 \times 10^{16} \text{ cm}^{-2}$ , and TEM-BF images of the stress distortion around the bubbles taken at (b) in-focus and (c) under-focus. The insets in (a) and (b) are corresponding FFT patterns. The orange dashed circle and arrows in (a) mark the He bubbles. (For interpretation of the references to colour in this figure legend, the reader is referred to the web version of this article.)

interstitial dislocation loops, thus, it is worth noting that the statistics about dislocation loops in Chapter 3.3 include the loops generated by the loop punching mechanism. In addition, the process of extruding lattice atoms to form vacancies for bubble growth is related to  $E_V^f$  (see Fig. 11). The decreased  $E_V^f$  of individual elements with increase of Pd content suggests that more self-interstitials can be extruded in 5Pd, 15Pd and 25Pd than that in 0Pd under the same He ion irradiation conditions, and the resulting bubble coarsening is correspondingly more significant in Pd-containing HEAs.

For another, He atoms are conducive to the nucleation of dislocation loops. Lucas et al. [56] found that He atoms in cascade collisions are more likely to appear at the region where interstitial clusters were formed. These He-interstitial clusters can provide nucleation sites for dislocation loops, thus facilitating their formation. Furthermore, the introduction of He atoms inevitably leads to an increase in vacancy migration energy [57], resulting in a significant reduction in the number of vacancies that can be recombined with interstitials. This leads to more surviving interstitials that can be involved in the formation and growth of dislocation loops [58]. To encapsulate, it can be inferred that Pd-containing HEAs can promote the annihilation of irradiation defects and inhibit the growth of dislocation loops in the absence of inert gas injection, but it is different in the case of He ion irradiation: more vacancies are created and occupied by He interstitials (due to the reduced  $E_V^f$  in Pd-containing HEAs), resulting in that the annihilation of point defects is suppressed, and the loop punch mechanism is promoted to produce more dislocation loops. Therefore, the CSRO and lattice distortion in Pd-containing HEAs may not play an effective role in inhibiting the formation and growth of irradiation defects under He ion irradiations.

#### 4.3. Contribution to irradiation-induced hardening of Pd-containing HEAs

The irradiation-induced hardening of metallic materials is closely related to the obstruction of gliding dislocations by defect clusters [42]. Due to the variability of He bubbles and dislocation loops in the HEAs with different Pd contents at three He-irradiation doses, their contributions to the irradiation-induced hardening are worth discussing in detail. The dispersed barrier-hardening (DBH) model can be used in this study to describe the increase in material strength caused by irradiation-induced defects [59], and generally the increase of yield stress has a linear relationship with hardening, states as Eqs. (10) and (11):

$$\Delta\sigma_y = \alpha M \mu b \sqrt{Nd} \quad (10)$$

$$\Delta H = K \Delta\sigma_y \quad (11)$$

where  $\Delta\sigma_y$  and  $\Delta H$  represent the increase of yield strength and hardness after irradiation, respectively;  $N$  and  $d$  represent the average size and number density of the defects (measured in TEM characterization), respectively;  $\alpha$  is the barrier strength factor that depends on the types of defects (0.2 for He bubbles, and 0.4 for dislocation loops);  $M$  is the Taylor factor ( $\sim 3.06$  for metallic materials with FCC structure);  $\mu$  is the shear modulus;  $b$  is the Burgers vector of gliding dislocations, and  $K$  is

the linear coefficient ( $\sim 3$  for austenitic alloys). As shown in Table 3, the difference between the hardening measured experimentally and predicted by the DBH model can be evaluated by using the shear modulus of 77 GPa for austenitic steels and Burger vector of  $(a_0/2) < 110>$  in austenitic steels [59]. Among them, according to the  $a_0$  data in Table 2, the Burger vector magnitude of 0Pd, 5Pd, 15Pd, and 25Pd HEAs can be calculated exactly as 0.253 nm, 0.254 nm, 0.258 nm, and 0.263 nm, respectively.

In addition, a specific parameter  $P_{He}$  ( $P_{He} = \Delta H_{He}/(\Delta H_{He} + \Delta H_l) \times 100\%$ ) was defined in this study to clarify the contribution of He bubbles in irradiation hardening of the HEAs with different Pd contents, as shown in Fig. 15. Under the same irradiation condition, the value of  $P_{He}$  increases gradually with the increase of Pd content. This phenomenon indicates that, in this study, the proportion of hardening caused by bubbles is positively correlated with Pd content, which is consistent with the statistical results (see Fig. 6) and the discussion in Chapter 4.1. In addition, the value of  $P_{He}$  also increases with the increase of He ion irradiation dose, which may be attributed to the saturation of dislocation loops [60,61] along with the increase of He concentration (the continuous increase of density and coarsening of He bubbles).

Notably, the hardening rates of Pd-containing HEAs in this study are numerically higher than those of many alloys or steels under similar He ion irradiation conditions, due to the fact that the vast majority of previously reported hardening behavior are considerably affected by the defect sinks of the irradiated materials. For example, Wu et al. [62] reported a significant suppression of irradiation hardening in nanograined 14YWT-ODS steel after He ion irradiation, which can be attributed to the strong sink strength provided by the high-density interfaces of grain boundaries and oxide precipitates. The difference is that the HEAs in this study can be considered as uniform single crystals in the irradiated region, excluding the influence factors such as grain boundaries and phase boundaries, hence, the irradiation hardening entirely depends on the inherent properties of the materials. Therefore, on the

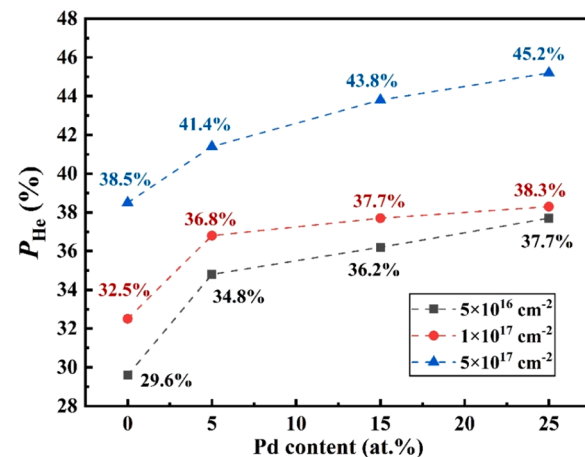


Fig. 15. The contribution of He bubbles in irradiation hardening ( $P_{He} = \Delta H_{He}/(\Delta H_{He} + \Delta H_l) \times 100\%$ ) of the HEAs with different Pd contents after He-irradiation to the fluences of  $5 \times 10^{16} \text{ cm}^{-2}$ ,  $1 \times 10^{17} \text{ cm}^{-2}$ , and  $5 \times 10^{17} \text{ cm}^{-2}$ .

Table 3

Hardening after irradiations measured by nanoindentation tests ( $\Delta H_n$ ), hardening predicted from DBH model contributed by He bubbles ( $\Delta H_{He}$ ) and dislocation loops ( $\Delta H_l$ ), and the proportion of the hardening caused by He bubbles ( $P_{He} = \Delta H_{He}/(\Delta H_{He} + \Delta H_l) \times 100\%$ ). The unit of the above hardness data is GPa.

Dose	$5 \times 10^{16} \text{ ions/cm}^2$				$1 \times 10^{17} \text{ ions/cm}^2$				$5 \times 10^{17} \text{ ions/cm}^2$			
	$\Delta H_n$	$\Delta H_{He}$	$\Delta H_l$	$P_{He}$	$\Delta H_n$	$\Delta H_{He}$	$\Delta H_l$	$P_{He}$	$\Delta H_n$	$\Delta H_{He}$	$\Delta H_l$	$P_{He}$
0Pd	1.67	0.53	1.26	29.6 %	2.11	0.75	1.56	32.5 %	2.94	1.11	1.77	38.5 %
5Pd	1.91	0.63	1.18	34.8 %	2.38	0.85	1.46	36.8 %	3.42	1.16	1.64	41.4 %
15Pd	1.99	0.68	1.20	36.2 %	2.44	0.89	1.47	37.7 %	3.71	1.28	1.64	43.8 %
25Pd	1.98	0.72	1.19	37.7 %	2.46	0.92	1.48	38.3 %	3.83	1.36	1.65	45.2 %

assumption that all samples in this study are not affected by the varying defect sinks, the irradiation hardening behavior can be described as the following synergistic and competitive relationship between bubbles and dislocation loops. At low irradiation doses ( $5 \times 10^{16} \text{ cm}^{-2}$  and  $1 \times 10^{17} \text{ cm}^{-2}$ ), dislocation loops generated by irradiation and loop punching mechanism are the main source of hardening, and Pd-containing HEAs show reduced hardening rates due to the demonstrated inhibition of dislocation loops growth in them. On the contrary, with the increase of irradiation dose ( $5 \times 10^{17} \text{ cm}^{-2}$ ), the bubbles continue to coarsen but loop size tends to plateau, indicating that the contribution of bubbles in hardening is becoming increasingly significant. The reduced  $E_V^f$  in Pd-containing HEAs promotes the coarsening of bubbles, resulting in a higher hardening rate in Pd-HEA than that of 0Pd.

## 5. Conclusion

To encapsulate, the present study reveals the effects of Pd alloying (accompanied by the replacement of Co) in He ion-irradiated FeCrNiCo HEAs on bubble evolution, and systematically evaluates the irradiation-induced hardening at several irradiation doses. Results indicate that the Pd-containing HEAs exhibit promoted bubble coarsening compared with the HEA without Pd alloying. This finding suggests that the strategy of using Pd alloying to introduce additional lattice distortions and chemical heterogeneities can improve the irradiation resistance of FeCrNiCo-system HEA in cases where irradiation defects are only caused by the aggregation of self-interstitials and vacancies. However, it is important to consider the reduced vacancy formation energy of Pd-containing HEAs in cases of irradiation with the introduction of high-concentration inert gas. Several important conclusions are as follows:

- (1) The alloying of Pd in FeCrNiCo high entropy alloy can impart additional lattice distortion and chemical fluctuations. 1 at.% Pd alloying (accompanied by the replacement of Co) increases the lattice constant of the FeCrNiCo by  $0.005 \text{ \AA}$ , and the chemical undulation increases from  $\sim 13\%$  of 0Pd to  $\sim 22\%$  of 25Pd.
- (2) The evolution of bubbles in this study follows two rules: Firstly, with the increase of irradiation dose, the average diameter and number density of bubbles increased. Secondly, under the same irradiation conditions, the average diameter of bubbles increases with the increase of Pd content, which can be attributed to the reduced vacancy formation energy in Pd-containing HEAs than that of FeCrNiCo without Pd alloying. In addition, 1 at.% Pd alloying (accompanied by the replacement of Co) reduces the vacancy formation energy of Fe, Cr, Ni by  $\sim 0.038 \text{ eV}$ .
- (3) A large number of perfect loops with  $b=1/2<110>$  were observed in the irradiated damaged region, which are produced by the combined contribution of cascade collision and loop punching mechanism, and the growth of dislocation loops is inhibited by Pd alloying.
- (4) The hardening mechanism in this study can be described as: the hardening is dominated by dislocation loops at low doses, and the loop growth is inhibited in the Pd-containing HEAs, so that they exhibit lower hardening rates. As the dose increases, the coarsened bubbles occupy the significant contribution of hardening, thus, due to the lower vacancy formation energy of the Pd-containing HEAs, they show higher hardening rates than the HEA without Pd alloying.

## Declaration of Competing Interest

The authors declare that they have no known competing financial interests or personal relationships that could have appeared to influence the work reported in this paper.

## Acknowledgments

The study was supported by the National Natural Science Foundation of China (12275010, 12335017, 11921006, 11975034, U21B2082 and U20B2025) and Beijing Municipal Natural Science Foundation (1222023). E.G. Fu acknowledges the support from the Science Fund for Creative Research Groups of NSFC, the Ion Beam Materials Laboratory (IBML) and Electron Microscopy Laboratory (EML) at Peking University.

## Supplementary materials

Supplementary material associated with this article can be found, in the online version, at doi:10.1016/j.actamat.2023.119404.

## References

- [1] S.J. Zinkle, G.S. Was, Materials challenges in nuclear energy, *Acta Mater.* 61 (3) (2013) 735–758.
- [2] G.S. Was, D. Pettit, S. Ukai, S. Zinkle, Materials for future nuclear energy systems, *J. Nucl. Mater.* 527 (2019), 151837.
- [3] J.L. Du, S.H. Jiang, P.P. Cao, C. Xu, Y. Wu, H.Q. Chen, E.G. Fu, Z.P. Lu, Superior radiation tolerance via reversible disordering-ordering transition of coherent superlattices, *Nat. Mater.* 22 (4) (2023) 442–449.
- [4] H. Kim, J.G. Gigax, C.J. Rietema, M.R. Chancey, J.K. Baldwin, Y.Q. Wang, S. A. Maloy, O. El Atwani, Void swelling of conventional and composition engineered HT9 alloys after high-dose self-ion irradiation, *J. Nucl. Mater.* 560 (2022), 153492.
- [5] Y. Chen, S. Wang, H. Feng, W.P. Li, B. Liu, J. Li, Y. Liu, P.K. Liaw, Q.H. Fang, Irradiation hardening behavior of high entropy alloys using random field theory informed discrete dislocation dynamics simulation, *Int. J. Plast.* 162 (2023), 103497.
- [6] H. Takamizawa, K. Hata, Y. Nishiyama, T. Toyama, Y. Nagai, The role of silicon on solute clustering and embrittlement in highly neutron-irradiated pressurized water reactor surveillance test specimens, *J. Nucl. Mater.* 556 (2021), 153203.
- [7] C.Y. Lu, L.L. Niu, N.J. Chen, K. Jin, T.N. Yang, P.Y. Xiu, Y.W. Zhang, F. Gao, H. B. Bei, S. Shi, M.R. He, I.M. Robertson, W.J. Weber, L.M. Wang, Enhancing radiation tolerance by controlling defect mobility and migration pathways in multicomponent single-phase alloys, *Nat. Commun.* 7 (2016) 13564.
- [8] T. Cheng, G. Wei, S.M. Jiang, J. Zhang, Y.Q. Wang, P. Liu, M.Q. Hong, E.K. Guo, F. Zhong, G.X. Cai, C.Z. Jiang, F. Ren, Enhanced resistance to helium irradiations through unusual interaction between high-entropy-alloy and helium, *Acta Mater.* 248 (2023), 118765.
- [9] B. Cantor, Multicomponent high-entropy Cantor alloys, *Prog. Mater Sci.* 120 (2021), 100754.
- [10] B. Cantor, I.T.H. Chang, P. Knight, A.J.B. Vincent, Microstructural development in equiatomic multicomponent alloys, *Mater. Sci. Eng. A Struct.* 375 (2004) 213–218.
- [11] S.J. Zinkle, J.T. Busby, Structural materials for fission & fusion energy, *Mater. Today* 12 (11) (2009) 12–19.
- [12] Q.Q. Ding, Y. Zhang, X. Chen, X.Q. Fu, D.K. Chen, S.J. Chen, L. Gu, F. Wei, H.B. Bei, Y.F. Gao, M.R. Wen, J.X. Li, Z. Zhang, T. Zhu, R.O. Ritchie, Q. Yu, Tuning element distribution, structure and properties by composition in high-entropy alloys, *Nature* 574 (2019) 223–227.
- [13] N.D. Tran, A. Saengdeepong, K. Suzuki, H. Miura, Y. Chen, Stability and thermodynamics properties of CrFeNiCoMn/Pd high entropy alloys from first principles, *J. Phase Equilibr. Diffus.* 42 (5) (2021) 606–616.
- [14] N.D. Tran, T. Davey, Y. Chen, DFT calculations of structural, magnetic, and stability of FeNiCo-based and FeNiCr-based quaternary alloys, *J. Appl. Phys.* 133 (4) (2023), 045101.
- [15] T.N. Yang, C.Y. Lu, G. Velisa, K. Jin, P.Y. Xiu, Y.W. Zhang, H.B. Bei, L.M. Wang, Influence of irradiation temperature on void swelling in NiCoFeCrMn and NiCoFeCrPd, *Scr. Mater.* 158 (2019) 57–61.
- [16] C.Y. Lu, T.N. Yang, K. Jin, G. Velisa, P.Y. Xiu, M. Song, Q. Peng, F. Gao, Y. W. Zhang, H.B. Bei, W.J. Weber, L.M. Wang, Enhanced void swelling in NiCoFeCrPd high-entropy alloy by indentation-induced dislocations, *Mater. Res. Lett.* 6 (10) (2018) 584–591.
- [17] Y. Tong, G. Velisa, S. Zhao, W. Guo, T. Yang, K. Jin, C. Lu, H. Bei, J.Y.P. Ko, D. C. Pagan, Y. Zhang, L. Wang, F.X. Zhang, Evolution of local lattice distortion under irradiation in medium- and high-entropy alloys, *Materialia* 2 (2018) 73–81.
- [18] S.J. Zhao, Y.W. Zhang, W.J. Weber, Engineering defect energy landscape of CoCrFeNi high-entropy alloys by the introduction of additional dopants, *J. Nucl. Mater.* 561 (2022), 153573.
- [19] C.M. Jimenez, L.F. Lowe, E.A. Burke, C.H. Sherman, Radiation damage in Pd produced by 1-3-MeV Electrons, *Phys. Rev.* 153 (3) (1967) 735–740.
- [20] R.E. Stoller, M.B. Toloczko, G.S. Was, A.G. Certain, S. Dwaraknath, F.A. Garner, On the use of SRIM for computing radiation damage exposure, *Nucl. Instrum. Methods B* 310 (2013) 75–80.
- [21] P.Y. Xiu, H.B. Bei, Y.W. Zhang, L.M. Wang, K.G. Field, STEM characterization of dislocation loops in irradiated FCC alloys, *J. Nucl. Mater.* 544 (2021), 152658.
- [22] L. Chaput, A. Togo, I. Tanaka, Finite-displacement computation of the electron-phonon interaction within the projector augmented-wave method, *Phys. Rev. B* 100 (17) (2019), 174304.

- [23] G. Kresse, Ab-initio molecular-dynamics for liquid-metals, *J. Non Cryst. Solids* 193 (1995) 222–229.
- [24] G. Kresse, J. Hafner, Ab-initio molecular-dynamics simulation of the liquid-metal amorphous-semiconductor transition in germanium, *Phys. Rev. B* 49 (20) (1994) 14251–14269.
- [25] G. Kresse, J. Furthmuller, Efficiency of ab-initio total energy calculations for metals and semiconductors using a plane-wave basis set, *Comput. Mater. Sci.* 6 (1) (1996) 15–50.
- [26] A. van de Walle, M. Asta, G. Ceder, The Alloy Theoretic Automated Toolkit: a user guide, *Calphad* 26 (4) (2002) 539–553.
- [27] J.P. Perdew, K. Burke, M. Ernzerhof, Generalized gradient approximation made simple, *Phys. Rev. Lett.* 77 (18) (1996) 3865–3868.
- [28] H.Q. Guan, S.S. Huang, J.H. Ding, F.Y. Tian, Q. Xu, J.J. Zhao, Chemical environment and magnetic moment effects on point defect formations in CoCrNi-based concentrated solid-solution alloys, *Acta Mater.* 187 (2020) 122–134.
- [29] Z.F. Hou, X.L. Wang, T. Ikeda, K. Terakura, M. Oshima, M. Kakimoto, Electronic structure of N-doped graphene with native point defects, *Phys. Rev. B* 87 (16) (2013), 165401.
- [30] S.J. Zhao, T. Egami, G.M. Stocks, Y.W. Zhang, Effect of d electrons on defect properties in equiatomic NiCoCr and NiCoFeCr concentrated solid solution alloys, *Phys. Rev. Mater.* 2 (2018), 013602.
- [31] P. Pulay, Convergence acceleration of iterative sequences. The case of SCF iteration, *Chem. Phys. Lett.* 73 (1980) 393–398.
- [32] Z.X. Su, J. Ding, M. Song, L. Jiang, T. Shi, Z.M. Li, S. Wang, F. Gao, D. Yun, E. Ma, C.Y. Lu, Enhancing the radiation tolerance of high-entropy alloys via solute-promoted chemical heterogeneities, *Acta Mater.* 245 (2023), 118662.
- [33] R.P. Zhang, S.T. Zhao, J. Ding, Y. Chong, T. Jia, C. Ophus, M. Asta, R.O. Ritchie, A. M. Minor, Short-range order and its impact on the CrCoNi medium-entropy alloy, *Nature* 581 (2020) 283–287.
- [34] X.F. Chen, Q. Wang, Z.Y. Cheng, M.L. Zhu, H. Zhou, P. Jiang, L.L. Zhou, Q.Q. Xue, F.P. Yuan, J. Zhu, X.L. Wu, E. Ma, Direct observation of chemical short-range order in a medium-entropy alloy, *Nature* 592 (2021) 712–716.
- [35] J. Ding, Q. Yu, M. Asta, R.O. Ritchie, Tunable stacking fault energies by tailoring local chemical order in CrCoNi medium-entropy alloys, *Proc. Natl. Acad. Sci. U. S. A.* 115 (36) (2018) 8919–8924.
- [36] W.Y. Chen, Z.G. Mei, L. Ward, B. Monsen, J. Wen, N.J. Zaluzec, A.M. Yacout, M. Li, *In-situ* TEM investigation of void swelling in nickel under irradiation with analysis aided by computer vision, *Acta Mater.* 254 (2023), 119013.
- [37] S. Shen, Z. Sun, L. Hao, X. Liu, J. Zhang, K. Yang, P. Liu, X. Tang, E. Fu, The mechanisms of inhibition effects on bubble growth in He-irradiated 316L stainless steel fabricated by selective laser melting, *Materials* 16 (11) (2023) 3922.
- [38] D. Taverna, M. Kociak, O. Stephan, A. Fabre, E. Finot, B. Decamps, C. Colliex, Probing physical properties of confined fluids within individual nanobubbles, *Phys. Rev. Lett.* 100 (2008), 035301.
- [39] W.Y. Chen, J.D. Poplawsky, Y.R. Chen, W. Guo, J.W. Yeh, Irradiation-induced segregation at dislocation loops in CoCrFeMnNi high entropy alloy, *Materialia* 14 (2020), 100951.
- [40] K. Ma, B. Decamps, A. Fraczkiewicz, F. Prima, M. Loyer-Prost, Inversion of dislocation loop nature driven by cluster migration in self-ion irradiated nickel, *Scr. Mater.* 208 (2022), 114338.
- [41] Y. Wang, S. Li, F. Chen, K. Yang, G. Ge, X. Tang, M. Fan, P. Huang, Unique dislocation loops distribution of AlCrFeNiTi<sub>x</sub> eutectic high-entropy alloys under high-temperature ion irradiation, *J. Alloy. Compd.* 958 (2023), 170373.
- [42] B.N. Singh, A.J.E. Foreman, H. Trinkaus, Radiation hardening revisited: role of intracascade clustering, *J. Nucl. Mater.* 249 (2–3) (1997) 103–115.
- [43] H. Trinkaus, B.N. Singh, A.J.E. Foreman, Segregation of cascade induced interstitial loops at dislocations: possible effect on initiation of plastic deformation, *J. Nucl. Mater.* 251 (1997) 172–187.
- [44] M.A. Mattucci, I. Cherubin, P. Changizian, T. Skippon, M.R. Daymond, Indentation size effect, geometrically necessary dislocations and pile-up effects in hardness testing of irradiated nickel, *Acta Mater.* 207 (2021), 116702.
- [45] S.K. Shen, F.D. Chen, X.B. Tang, J.W. Lin, G.J. Ge, J. Liu, Effects of carbon doping on irradiation resistance of Fe38Mn40Ni11Al4Cr7 high entropy alloys, *J. Nucl. Mater.* 540 (2020), 152380.
- [46] W.D. Nix, H.J. Gao, Indentation size effects in crystalline materials: a law for strain gradient plasticity, *J. Mech. Phys. Solids* 46 (3) (1998) 411–425.
- [47] R. Kasada, Y. Takayama, K. Yabuuchi, A. Kimura, A new approach to evaluate irradiation hardening of ion-irradiated ferritic alloys by nano-indentation techniques, *Fusion Eng. Des.* 86 (9–11) (2011) 2658–2661.
- [48] X.F. Liu, C.K. Tse, Impact of degree mixing pattern on consensus formation in social networks, *Phys. A* 407 (2014) 1–6.
- [49] H. Trinkaus, B.N. Singh, Helium accumulation in metals during irradiation – where do we stand? *J. Nucl. Mater.* 323 (2) (2003) 229–242.
- [50] H.W. King, Quantitative size-factors for metallic solid solutions, *J. Mater. Sci.* 1 (1966) 79–90.
- [51] F. Tuomisto, I. Makkonen, J. Heikinheimo, et al., Segregation of Ni at early stages of radiation damage in NiCoFeCr solid solution alloys, *Acta Mater.* 196 (2020) 44–51.
- [52] C. Dai, P. Saidi, B. Langelier, Q. Wang, C.D. Judge, M.R. Daymond, M. Mattucc, Radiation-induced segregation on dislocation loops in austenitic Fe-Cr-Ni alloys, *Phys. Rev. Mater.* 6 (2022), 053606.
- [53] Y.W. Zhang, X. Wang, Y.N. Osetsky, Y. Tong, R. Harrison, S.E. Donnelly, D. Chen, Y.Q. Wang, H.B. Bei, B.C. Sales, K.L. More, P.Y. Xiu, L.M. Wang, W.J. Weber, Effects of 3d electron configurations on helium bubble formation and void swelling in concentrated solid-solution alloys, *Acta Mater.* 181 (2019) 519–529.
- [54] Y. Li, G. Ran, Y. Guo, Z. Sun, X. Liu, Y. Li, X. Qiu, Y. Xin, The evolution of dislocation loop and its interaction with pre-existing dislocation in He<sup>+</sup>-irradiated molybdenum: *in-situ* TEM observation and molecular dynamics simulation, *Acta Mater.* 201 (2020) 462–476.
- [55] J.H. Evans, The role of implanted gas and lateral stress in blister formation mechanisms, *J. Nucl. Mater.* 76–77 (1978) 228–234.
- [56] G. Lucas, R. Schaublin, Helium effects on displacement cascades in alpha-iron, *J. Phys. Condens. Mater.* 20 (41) (2008), 415206.
- [57] N. Hashimoto, S. Sakuraya, J. Tanimoto, S. Ohnuki, Effect of impurities on vacancy migration energy in Fe-based alloys, *J. Nucl. Mater.* 445 (1–3) (2014) 224–226.
- [58] E. Wakai, Y. Miwa, N. Hashimoto, J.P. Robertson, R.L. Klueh, K. Shiba, K. Albiko, S. Furuno, S. Jitsukawa, Microstructural study of irradiated isotopically tailored F82H steel, *J. Nucl. Mater.* 307 (2002) 203–211.
- [59] N.A.P.K. Kumar, C. Li, K.J. Leonard, H. Bei, S.J. Zinkle, Microstructural stability and mechanical behavior of FeNiMnCr high entropy alloy under ion irradiation, *Acta Mater.* 113 (2016) 230–244.
- [60] A.R. Warwick, R. Thomas, M. Boleininger, O. Kot, G. Zilahi, G. Ribarik, Z. Hegedues, U. Lienert, T. Ungar, C. Race, M. Preuss, P. Frankel, S.L. Dudarev, Dislocation density transients and saturation in irradiated zirconium, *Int. J. Plast.* 164 (2023), 103590.
- [61] K. Ma, B. Decamps, L.Z. Huang, R.E. Schaublin, J.F. Loffler, A. Fraczkiewicz, M. Nastar, F. Prima, M. Loyer-Prost, Impact of micro-alloying in ion-irradiated nickel: from the inhibition of point-defect cluster diffusion by thermal segregation to the change of dislocation loop nature, *Acta Mater.* 246 (2023), 118656.
- [62] Z.F. Wu, L.D. Xu, H.Q. Chen, Y.X. Liang, J.L. Du, Y.F. Wang, S.L. Zhang, X.C. Cai, B. R. Sun, J. Zhang, T.D. Shen, J. Wang, E.G. Fu, Significant suppression of void swelling and irradiation hardening in a nanogranulated/nanoprecipitated 14YWT-ODS steel irradiated by helium ions, *J. Nucl. Mater.* 559 (2022), 153418.